Seasonal and episodic runup variability on a Caribbean reef-lined beach

Thibault Laigre, Yann Balouin, Alexandre Nicolae-Lerma, Manuel Moisan, Nico Valentini, D. Villarroel-Lamb, Ywenn De la Torre

Seasonal and episodic runup variability on a Caribbean reef-lined beach

T. Laigre[1,2], Y. Balouin[3], A. Nicolae-Lerma[4], M. Moisan[1], N. Valentini[3], D. Villarroel-Lamb[2], Y. De La Torre[1]

[1]BRGM, Parc d'activités Colin - La Lézarde, 97170 Petit Bourg, Guadeloupe, France, [2]The University of the West Indies, St Augustine Campus, Trinidad and Tobago, [3]BRGM - Univ. Montpellier, 1039 Rue de Pinville, 34000 Montpellier, France, [4]BRGM, Parc technologique Europarc, 24 Av. Léonard de Vinci, 33600 Pessac

Corresponding author: Thibault Laigre (t.laigre@brgm.fr)

Key Points:

- A camera derived time serie of 2 years and 10 months is used to evaluate processes involved on daily maximum runup
- Steric induced annual sea level periodicity modulate the daily maximum runup, tide level acts on short waves propagation through the reef
- Storms-induced runup is highly modulated by annual sea level periodicity and tidal level

Abstract

Many low-lying coastlines are exposed to overwash and marine flooding during large wave events and the role of coastal ecosystems in reducing these hazards is more and more cited. The proposed article deals with the assessment of processes involved in runup-induced coastal flooding over two years and 10 months at Anse Maurice, a reef-fringed pocket beach located in Guadeloupe Island, in the Caribbean region. Daily maximum marine inundation was assessed using a fixed video system and two hydrodynamic measurements campaigns were organised to monitor local wave transformation through the reef system. Daily Highest Runups (DHR) remains primarily correlated to individual storm events as extreme runups are observed in correlation with storm swells. However, results evidenced that storm runup intensity is highly modulated by (1) the annual periodicity of sea level (24% of the global runup variability) showing minimums in May and maximums in November and (2) the tidal level influencing short waves and infragravity waves propagation into the reef flat. Those variabilities determine the reef submergence, an important parameter involved in wave transformation over reefs. This leads to different runup responses for similar incident wave conditions. For example, most of the winter storm events only induce moderate intensity runup while cyclonic events with the same swell intensity generate more extreme runups. The upperbeach vegetation also clearly influences the maximum swash excursion at the beach and potential back beach flooding by swash processes. This study brings new comprehensive elements on runup beahavior and nearshore processes at different timescales on reef-lined beaches.

Plain Language Summary

Small Caribbean islands are highly vulnerable to coastal flooding hazard. The role of ecosystems its mitigation is increasingly emphasized. We assess the various physical processes involved in beach inundation at a reef-lined beach located in Guadeloupe Island in the Caribbean. A pluri-annual dataset from a fixed camera and two monthly hydrodynamic campaigns are used. This work highlights the implication of processes involved in wave-induced coastal inundation (runup) from annual to hour time scale. Seasonal variations are the consequence of fluctuations in sea temperature and salinity which act on water bodies expansion (called steric effect) and our results indicate that they can be responsible for 24% of runup variability. On shorter time scales, tides have an effect on wave propagation over the coral reef directly influencing residual agitation at shoreline level. Thus, storms events which are responsible for peaks in coastal inundation have an impact that is greatly modulated both by the annual periodicity of sea level and by the short timescale tidal level. The effect of tide is well-known, however the effect of annual periodicity of sea level had never been demonstrated, so this results brings new elements to understand wave induced coastal inundation in the context of reef-lined beaches.

1 Introduction

Small Caribbean Islands are highly vulnerable to coastal flooding. On the one hand since the limited space and topographical constraints have oriented human development near to the coastal areas and, and on the other hand because the Caribbean region is exposed to strong hydrodynamic events through winter storms and hurricanes. The strength of the latter is predicted to rise in the near future (Knutson et al., 2020) and in association with other effects of climate change like sea-level rise, the frequency of flooding events is expected to rise in the next decades (Vitousek et al., 2017) with its concomitant impact on human assets (Ferrario et al., 2014).

Considering hydrodynamic forcing, extreme sea-levels and direct wave impact are the principal parameters involved in coastal inundation. Short-term mean sea-level variability is related to both predictable parameters (e.g., tidal cycles) and stochastic parameters (e.g., wave and wind setup, storm surge). In the Caribbean maximum coastal flooding events are related to cyclones (Rueda et al., 2019). Sea-level fluctuations on a yearly basis are also well-known and may be the consequence of the association of seasonal variations of atmospheric pressure and winds, steric effect, ocean circulation (Torres and Tsimplis, 2012) and water mass transfer from the continents (ice sheets, glaciers or rivers). Other forcings with several years or even decennial cycles also modulate sea level such as El Niño Southern Oscillation (ENSO) (Chelton and Enfield, 1986) or solar activity (Valle-Levinson and Martin, 2020). In addition, sea level is expected to rise in the near future with geographically varying amplitudes (e.g. Losada et al., 2013, Stammer et al., 2013; Torres and Tsimplis, 2013; Slangen et al., 2014; Le Cozannet et al., 2020; Wang et al., 2021) which will inevitably affect coastal inundation (Storlazzi et al., 2018).

In opposition, there is strong evidence that healthy coastal ecosystems, and in particular tropical ecosystems, can substantially reduce coastal hazards (Spalding et al., 2014; Guannel et al., 2016). At reef-lined coasts, the attenuation of the impact of coastal hazards depends mainly on coral reef morphology (e.g., slope, width, structural complexity) and hydrodynamic forcing (e.g., water level) whose main effect is to dampening incident wave energy. Incident wave conditions show significant transformation across reefs both in intensity, as well as, in spectral dispersion. Wave propagation on coral reefs produces a tremendous energy dissipation (Harris et al., 2018) and a switch in waves spectrum from high Short Waves (SW, typically frequency > 0.04 Hz) to Infragravity Wave (IG, 0.004 < frequency > 0.04 Hz) and Very Low Frequency waves (VLF, frequency < 0.004 Hz) undulations often leading to a low frequency undulation dominance at the shoreline (Péquignet et al., 2009; Pomeroy et al., 2012; Roeber and Bricker, 2015; Cheriton et al., 2016 and 2020; Sous et al., 2019). In consequence, IG waves may be responsible of maximum runup, overwash events (Ford et al., 2013, Quataert et al., 2015, 2020; Roeber and Bricker, 2015) and beach erosion (Bertin et al., 2018). The two main processes considered in wave transformation over the reef are (1) nonlinear interactions in shallow areas: as short waves breaks, bound long waves are released and continue to propagate to the shore as a free wave (Longuet-Higgins and Stewart, 1962) and (2) breakpoint forcing on the reef crest which are linked to the variation of wave setup induced by wave groups generating a setup wave in phase with group waves (Symonds et al., 1982).

A meta-analysis conducted by Ferrario et al., (2014) estimated that even if results remain site-specific, coral reef assemblages dissipate an average of 97% of incident wave energy at the shoreline. Simultaneously, a fraction of incident SS is transformed to lower frequency waves: IG and VLF (Péquignet et al., 2014). This switch in energy frequency bands is commonly observed at reef-lined beaches (Masselink et al., 2019) but strongly depends in a one hand of hydrodynamic conditions (tidal level, atmospheric surge and wave parameters) and in a second hand of geomorphological characteristics of the reef platform (depth, width, front reef slope, channels, reef flat width and depth). The biological composition of the coral assemblage and may also have an impact on hydrodynamic with the most complex structures representing a stronger obstacle (e.g. Acropora species). IG and VLF may also be amplified by resonance when the energy frequency is near the reef natural frequency, depending in reef flat properties and in particular width and depth (Péquignet et al., 2009, 2014; Pomeroy et al., 2012; Gawehn et al., 2016). Several recent studies dealt specifically with runup and coastal flooding in a coral reef

context. Buckley et al. (2018) and Ning et al. (2019) focused on physical mechanisms conducting laboratory experiments in association with a numerical modeling for the latter. Both supported the hypothesis of a reduction of runup by the coral reef (30 % compared to smooth bed). Roelvink et al. (2021) carried out a laboratory experiment on optimization of reef restoration to reduce flooding where the results postulated the effectiveness of broad and shallow restorations. However, as reefs possess highly variable physical characteristics, particularly front reef slope, roughness and reef flat dimensions (width, and shallowness) their response to incident agitation also differs accordingly. A bayesian-based meta-model was developed to predict runup response in a wide panel of reef settings. It emerges that waves, water levels and reef width are the main parameters involved in backreef runup (Pearson et al., 2017). Nervertheless, high-resolution observations of runup on field are scarce. A recent study presents a runup dataset of a duration close to the year (Melito et al., 2022) but to the authors knowledge no study propose a continuous multi-years survey dataset preventing analysis of runup variability at daily to pluriannual time scale.

This study investigates the parameters involved in runup on a reef fringed pocket beach typical of the Lesser Antilles from varying time scales: an event level to years. The objectives are: (1) to identify the parameters most related to wave runup (such as sea level and incident wave conditions) on a pluri-annual basis: (2) to analyze the relative importance of these parameters (in particular wave setup, SS, IG and VLF) in daily runup fluctuations, and (3) to identify and quantify runup mitigation by the reef by evaluating wave transformation through the reef and by analyzing the effects of local longshore variability. Camera observations. were used for the medium to long-term analysis (seasonal to pluri-annual), and data from local hydrodynamic measurements were used for the analysis on short to medium-term (event scale to month scale). This study brings new elements on the observations of runup on reef-lined beaches. In particular through the use of a long-term video derived dataset in combination with onsite measurements to analyze sea level and runup component from daily to annual scale.

2 Study area and methodology

2.1 Study site

Anse Maurice is located in the Guadeloupe Island (France) in the Lesser Antilles (Figure 1 (a) and (b)). It is a small beach about 200 m long and between 5 and 20 m wide. Shoreline monitoring indicates a chronic erosion with a net retreat of 20 m on average between 1950 and 2013 (Guillen et al., 2017).

The beach is bordered by a fringing reef mainly composed by *Acropora Palmata* dead colonies covered by algae. However, some complex structures of several meters in height are still observed (Figure 1 (e)). The reef flat is composed of discontinuous dead coral structures of about one meter in height and several meters in width as well as small colonies of living branching and encrusting corals. In the southern part of the site, an eastward channel is identifiable where the coral structures are sparser and deeper (Figure 1 (b)).

The upper beach is covered by heterogeneous patches of vegetation: crawling vegetation mainly represented by *Ipomoea Pes-Caprae* in the front line and shrubs like *Coccoloba Uvifera* in the back line (Figure 1 (d)). Several exogenous coconut trees are also present on-site.

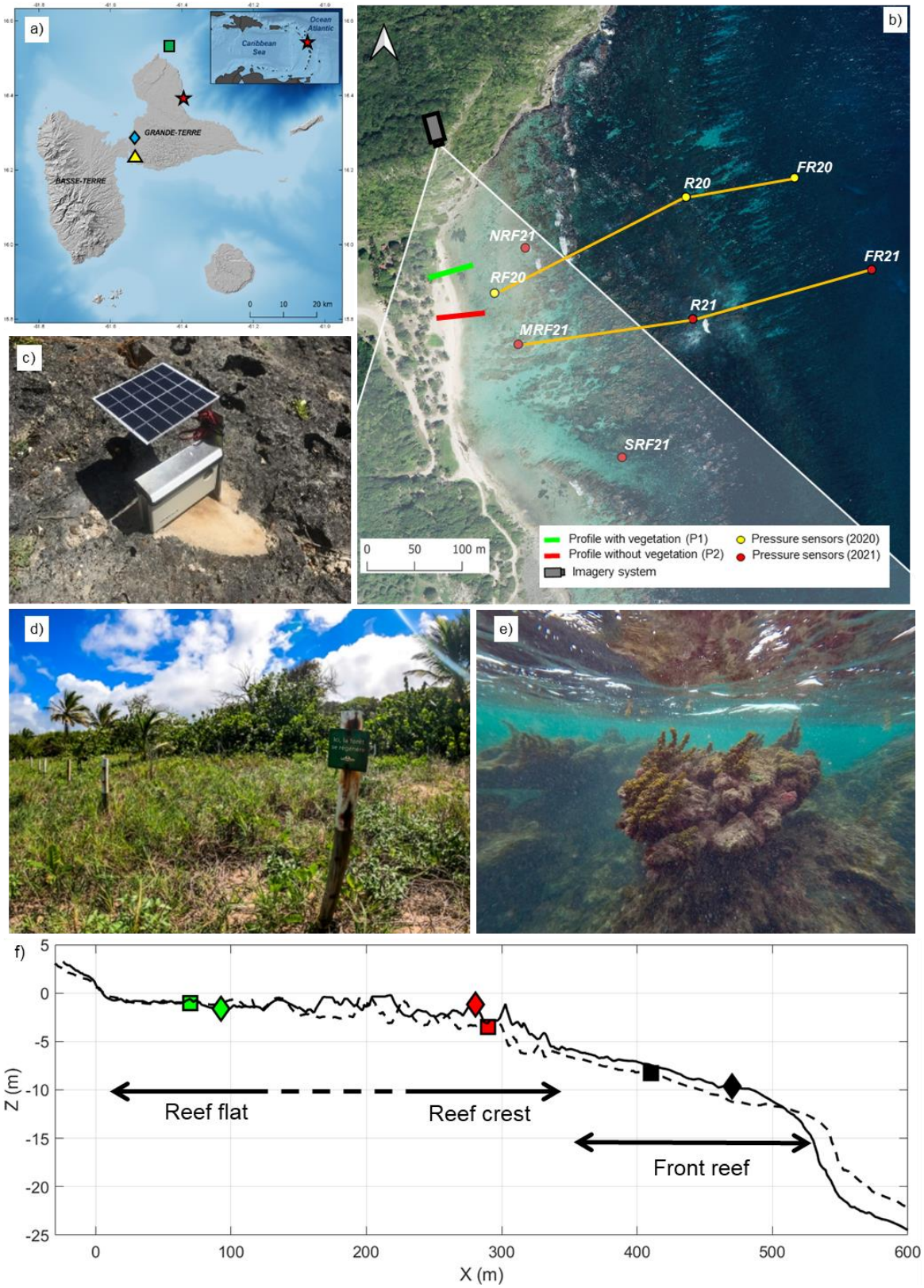

Figure 1. (a) Location of Guadeloupe Island in the Caribbean and Anse-Maurice beach (red star) at the East of the Island. Markers indicate the location of main regional datasets: ADCP (green

square), meteorological station (blue diamond) and tide gauge (yellow triangle). (b) Anse-Maurice beach orthophotography with location of instruments. (c) Imagery system installed at Anse-Maurice. (d) Upperbeach vegetation at the Anse Maurice. (e) Anse Maurice reef crest showing a dead Acropora Palmata colony covered with algae. (f) Instrumented cross-reef profiles with reef flat (green), reef crest (red) and front reef (black) sensors for 2020 campaign (dashed line and squares) and 2021 campaign (solid line and diamonds).

Beach vegetation at the Anse-Maurice site is very impacted by human activities and particularly by trampling and goat grazing. Obviously, lower layers of vegetation are the most touched, which obstruct the development of crawling vegetation and seedlings. Consequently, in the medium-term, the growth of a new generation of trees is then being hampered and the soil is more subject to erosion. Therefore, the French Forestry Agency (ONF) had implemented several revegetation enclosures (https://www.carib-coast.com/en/news/anse-maurice-actions-carried-out-on-this-pilot-site-of-the-carib-coast-project/). Those features consist of simple wooden sticks connected by wire mesh to avoid human trampling and goat grazing which facilitate the recovery of vegetation. After a few months, the effects are noticeable and a dense vegetation maybe restored after a few years (Johnston and Ellison, 2014; Ellison, 2018). Even in a deteriorated state, the role of the reef and upperbeach vegetation on coastal flooding attenuation is expected, although this has not been locally evaluated.

The site is a wave-dominated beach, offshore swells vary greatly with an annual mean of 1.2 m. It is exposed to strong Atlantic swells with most of the storms occurring during the winter season from December to March; these swells mainly comes from the North to East-North-East direction. The site is also subject to cyclonic events from July to November which can generate the most powerful waves reaching the island. Nevertheless, due to the site exposition, only swells from North to East direction impact it directly. Besides these two highly energetic wave regimes, waves generated by the trade winds affect the region all year round with wave heights ranging from 0.5 to 2 m (Reguero et al., 2013; CEREMA, 2021). The flooding risks are primarily associated to the occurrence of tropical cyclones (Krien et al., 2015; Rueda et al., 2017).

The area shows a semi-diurnal microtidal range, with diurnal and mixed inequality, a mean amplitude of 0.25 m and ranging from 0.1 m during neap tides to 0.7 m during spring tides (SHOM 2020).

Seasonal sea-level changes are the combined result of atmospheric pressure variations, wind effect and steric expansion. Atmospheric pressure annual variations in the Caribbean are the consequence of Inter Tropical Convergence Zone (ITCZ) displacement, surface winds are dominated by the Trade winds and steric expansion is due to temperature, salinity and pressure change of seawater (Torres and Tsimplis, 2012; Chadee and Clarke, 2015). In Guadeloupe Island in particular, the barometric effect is not significant (< 0.01m) and most annual sea-level variations are the consequence of steric effects with an amplitude of 0.15 m in Guadeloupe Island, maximas on October and minimas in April (Torres and Tsimplis, 2012).

2.2 Field measurements

2.2.1 Video derived coastal state indicators

Video systems are nowadays widely used to evaluate coastal evolution and coastal hydrodynamics allowing the quantitative acquisition of optical signatures of shoreline position

(Holman and Stanley, 2007, Plant et al. 2007, Valentini and Balouin, 2020), nearshore morphologies (Bergsma and Almar, 2018; Aarninkhof, 2004), wave characteristics (Almar et al., 2008), surf zone wave-induced current (Rodríguez –Padilla et al., 2021) and wave runup (Salmon et al., 2007; Valentini et al., 2019). Recently, low-cost webcams are increasingly used (Andriolo et al., 2019; Paquier et al., 2020; Valentini et al., 2020) and have proven their ability to acquire reliable data at an affordable price.

In this study, two low-cost Solarcam© camera systems were implemented in April 2019 to monitor coastal evolution (Figure 1 (b) and (c)). Each system comprises an 8 MP resolution smartphone protected by a waterproof housing, and powered by a solar panel. The whole system is entirely autonomous as it is programmed to record an image every 10 minutes, and is able to record short videos (Valentini and Balouin, 2020). This low-cost device showed its applicability on several purpose (Valentini and Balouin, 2020; Moisan et al., 2021) but it is inadequate to study nearshore hydrodynamic as it is not able to record videos with sufficient duration and frequency.

A dataset of 2.5 years and 10 months has been analysed in this study. The images from the cameras were calibrated with ground control points using the Holland et al. (1997) methodology in order to obtain data in real-world scale. This rectification processing allows the transformation of U,V image coordinates to X,Y,Z world coordinates and allows the quantitative assessment of coastal indicators. After rectification, timestacks were generated corresponding to the location of profiles (Figure 1(b)). A timestack represents the plotted evolution over time of a particular line of pixels. Morphological markers like the limit between sand and vegetation, or the limit formed by marine debris are easily identifiable on images and may be monitored overtime with timestacks. For example, brown patterns located at the limit between sand and water (e.g., the shoreline) are sargassum algae deposits. Those are effective markers of maximum swash events on timestacks because they present a clear colorimetric contrast with the sand. During storm events, this data is useful to identify instantaneous runup position and maximum runup limit at upperbeach, potentially generating back beach inundation. This limit (Daily Highest Runup noted DHR) has been identified and extracted on a daily basis. A better precision was obtained by detecting the swash limit on raw oblique images rather than timestacks because of their rapid evolution. Vegetation limit evolution is more stable and was directly extracted from timestacks. To obtain a runup value, the position of the swash limit on profile is correlated with the local Digital Elevation Model (DEM). The latter is derived from RTK-GPS monitoring for the topography and from Lidar dataset (SHOM, 2016) for the bathymetry. The DHR elevation is then expressed in the local reference system (IGN88). For this research, two timestacks will be used and compared, the first one in a profile with dense upperbeach vegetation (the northern one on Figure 1 (b), hereafter called P1) and the other in a profile with limited upperbeach vegetation (hereafter called P2). The mean pixel resolution on each profile is respectively 0.15 m and 0.19 m.

2.2.2 Hydrodynamic data and instrumentation

Offshore wave conditions were extracted from the mesoscale MARC model outputs available online. MARC is a reanalysis of the WAVEWATCH III® model at a regional scale; simulation results are provided by the IFREMER and available in real time (http://umr-lops.org/marc). Wave parameters (significant wave height H_s, peak period Tp and direction at the peak Dp) were extracted at the location of Acoustic Doppler Current Profiler (ADCP) sensor for validation of MARC model outputs (Figure 1 (a)). The ADCP (©Nortek Aquapro) was installed at 50 m depth

to measure offshore waves from September to December 2020 (Figure 1 (a)). Beside a strong correlation the ADCP measurements and the MARC model ($R^2 = 0.90$), an observed difference depending on the wave conditions exist (a greater variance was observed on extreme wave conditions). This observation on offshore waves conditions is commonly made when comparing instrumental data and models (e.g. Castelle et al., 2015). It was decided to apply a correction method on the distribution of wave conditions and thus, a quantile by quantile correction had been applied (Charles et al., 2012). The overall correlation slightly increase after the correction ($R^2 = 0.92$).

Furthermore, the method used by Masselink et al., 2016 was applied to detect and isolate storms. On the H_s dataset, the percentile 95% $H_{s\ 95\%}$ (here 2.3 m) was extracted and identified as storm peaks. The upcrossing and downcrossing on the 75% percentile defines the beginning and end of storms (here 1.84 m).

In order to compare the DHR obtained from the video system, daily maximum wave parameters were extracted from corrected MARC model outputs. Actually, the daily H_s maximum value was extracted as well as Tp and Dp at the time of maximum wave height. A daily value of sea level from Pointe-à-Pitre tide gauge (Figure 1(a)) was extracted following the same methodology. Data from the tide gauge are provided by the French Hydrographic Service (SHOM) and available on the REFMAR database (www.http://data.shom.fr).

Two campaigns of hydrodynamic measurements were organized during the North Atlantic cyclonic season of 2020 and 2021. Sensor positions for both campaigns have been chosen according to reef characteristics so they can be compared by the relative cross-shore position on the reef. The former started on September 30th and lasted until October 29th 2020 (30 days). Three Wisens Wave pressure sensors (NKE instrument©) were installed along a cross-shore profile (see Figure 1 (b)): the first one on the front reef, the second one on the reef crest and the last one in the reef flat. The second campaign started on August 26th and lasted until October 01st 2021 (31 days). Five pressure sensors were installed: three on a cross-shore profile as for the first campaign and two on both sides of the transect in the reef flat in order to evaluate the effect of reef longshore variability on wave transformation. Thus, one was placed at the North of the reef flat in a shallow and sheltered area close to 2020 reef flat sensor position and the second at the South of the reef flat in front of a clear depression of the reef.

For both campaigns, pressure sensors and the ADCP were set up to record bursts of 2048 readings at a sampling frequency of 2 Hz (~17 minutes duration) every hour. Table 1 details the sensors setup. Firstly, the effect of atmospheric pressure on raw pressure records were removed with the help of 3 hourly data from MeteoFrance station at le Raizet Airport at approximately 20 km of the site. From filtered datasets one-dimensional frequency spectra $S(f)$ was then estimated with the help of a Welch's averaged periodogram method with windows of half burst length and 50% overlapping. Then, for each burst and for SW, IG and VLF frequency band, several statistical parameters were extracted. Cutoff frequencies were chosen in agreement with previous works with SW: 0.2 > frequency > 0.04 Hz, IG: 0.004 < frequency > 0.04 Hz and VLF: frequency < 0.004 Hz (e.g. Péquignet et al., 2009; Cheriton et al., 2016 and 2020; Quataert et al., 2020). Root-mean-squared wave height (H_{rms}) which can be described as:

$$H_{rms} = \sqrt{8 \int_{f2}^{f1} S(f) df}$$

With $f1$ and $f2$ the lower and upper frequency limits. The peak period Tp value for each band represents the peak $1/fp$ with fp the frequency of the peak of energy. The H_{rms} transmission

coefficient between the front reef and the reef flat was also calculated on each frequency band. It represent the ratio of H_{rms} measured by the sensors in the reef flat (transmitted) and H_{rms} measured by the sensors on the front reef (incident) (Lugo-Fernández et al., 1998; Costa et al., 2016; Escudero et al., 2020). The transmission is then in percentage, values inferior to 100% reflect an attenuation between the front reef and the reef flat and values above 100% reflect an amplification.

The setup in the reef flat was also extracted from measurements and calculated following Vetter et al., 2010 methods as:

$$\eta = h_{rf} - h_{fr} - (bt + c)$$

With η the wave-induced setup in the reef flat, h_{rf} and h_{fr} respectively the burst-averaged water levels for the reef flat and the front reef sensor. b and c are empirically chosen and used to account for drifts from pressure transducers over time and offset respectively.

A set of statistical analysis was performed to identify and quantify the dependency between variables. Squared Pearson coefficient was calculating when comparing two linear random variables with linear distribution (such as H_{rms}, Tp, sea level) defined in Fisher (1958) as:

$$R^2(A,B) = \left(\frac{1}{N-1}\sum_{i=1}^{N}\left(\frac{A_i\mu_A}{\sigma_A}\right)\left(\frac{B_i\mu_B}{\sigma_B}\right)\right)^2$$

With A and B the variables, N the number of observations, μ_A the mean of A and μ_B the mean of B, σ_A as the standard deviation of A, and σ_B the standard deviation of B.

In order to compare a linear random variable with a circular random variable (such as Dp) a circular-linear correlation was performed as defined in Mardia and Jupp (2000) as:

$$R^2(A,\theta) = \frac{r_{Ac\theta}^2 + r_{As\theta}^2 - 2r_{Ac\theta}r_{As\theta}r_{cs\theta}}{1 - r_{c\theta s\theta}^2}$$

With

$$r_{Ac\theta} = corr(A, cos\ \theta)$$
$$r_{As\theta} = corr(A, sin\ \theta)$$
$$r_{c\theta s\theta} = corr(sin\ \theta, cos\ \theta)$$

A and θ are respectively the linear random variable and the circular random variable.

Both coefficients (Pearson and Circular-linear) range between 0 and 1, the association between variable is stronger with greater values. In this study correlations above 0.2 were considered as significant and correlations above 0.6 as strong.

Sensor name	Deployment period	Active duration (days)	Burst sampling	Frequency (Hz)	Depth (m)	Relative distance to reef crest (m)
FR20	Sept-Oct 2020	31	1 burst/ hour	2	6	-170
R20	Sept-Oct 2020	31	1 burst/ hour	2	3,65	-60
RF20	Sept-Oct 2020	31	1 burst/ hour	2	1,5	170
FR21	Aug-Sept 2020	37	1 burst/ hour	2	8,9	-200
R21	Aug-Sept 2020	37	1 burst/ hour	2	2,7	0
RF21	Aug-Sept 2020	37	1 burst/ hour	2	1	175
NRF21	Aug-Sept 2020	35	1 burst/ hour	2	1	150
SRF21	Aug-Sept 2020	36	1 burst/ hour	2	2,6	115

Table 1. Sensors setup during field campaigns. Sensors names correspond to the positon over the reef and the year (FR: front reef, R: reef crest, RF: reef flat, NRF: north reef flat and SRF: south reef flat).

3. Results

3.1 Mid/long-term observations

Figure 2 presents observations over 1045 days. During this period, on corrected MARC model dataset, offshore H_s exceeded 3 m for 16 times, with three of these events over 4 m. The first was a winter storm with a peak on January 10th 2020 and the two others were cyclonic events peaking on July 20th 2020 and on September 20th 2020 related to Hurricane Teddy circulating at 800 km to the East of Guadeloupe Island (NHC, 2021). Waves generated by cyclonic events are easily identifiable because their direction evolves quickly (generally from East or South-East to North) and those are the only strong swells from the East direction. Winter events are strictly from the North or North-East and show the greater wave periods as those are mostly generated in North Atlantic mid-latitudes.

Figure 2 (c) and (d) present timestacks over the same period at two cross-shore locations represented by red lines on Figure 1 (b). As it is mentioned in Section 2.2.1, the northern timestack is located in an area with dense upperbeach vegetation mostly comprising of *Ipomoea Pes-Caprae*. The southern timestack is in an area where upperbeach vegetation is less developed and located more landward as a consequence of human trampling. Vegetation limit and maximum swash excursion are plotted. The influence of tide cycles is noticeable on the shoreline during calm period as for example on the first quarter of both stacks. The vegetation, only present on the northern timestack in Figure 2 (c), shows an evolution in vegetation density, materialized by variations from green color to yellowish behind the vegetation limit. The vegetation limit on the coastal border (plotted in green on Figure 2 (c)) shows slow growth periods interrupted by abrupt retreat in concomitance with extreme storm events. Two remarkable moves appear with net retreats of 3 and 4 m. The first one correspond to the event 8 and the second to event 15 on Table 2.

Seven major swash excursions events are easily identified on the timestacks: corresponding to events 1, 2, 7, 8, 13, 15, 16 and 17 on Table 2. The event number 8 (September 17^{h} 2020) is the most extreme with maximum swash excursion of 12 m inland, and corresponding to runup exceeding 1.5 m, this event corresponds to the passage of Teddy Hurricane offshore Guadeloupe Island. All high runup events occurred during the cyclonic season and storms occurring during

winter and even the most extreme ones as the event number 4 in January 2020 seems to have not generated major swash excursion.
Runup elevation (figure 2 (e)) has the same mean value for both vegetated and unvegetated profiles. However, the profile with vegetation has a maximum runup of 1.42 m when the profile without vegetation has a maximum of 1.54 m, thus an exceedance of 0.12 m when vegetation is absent.

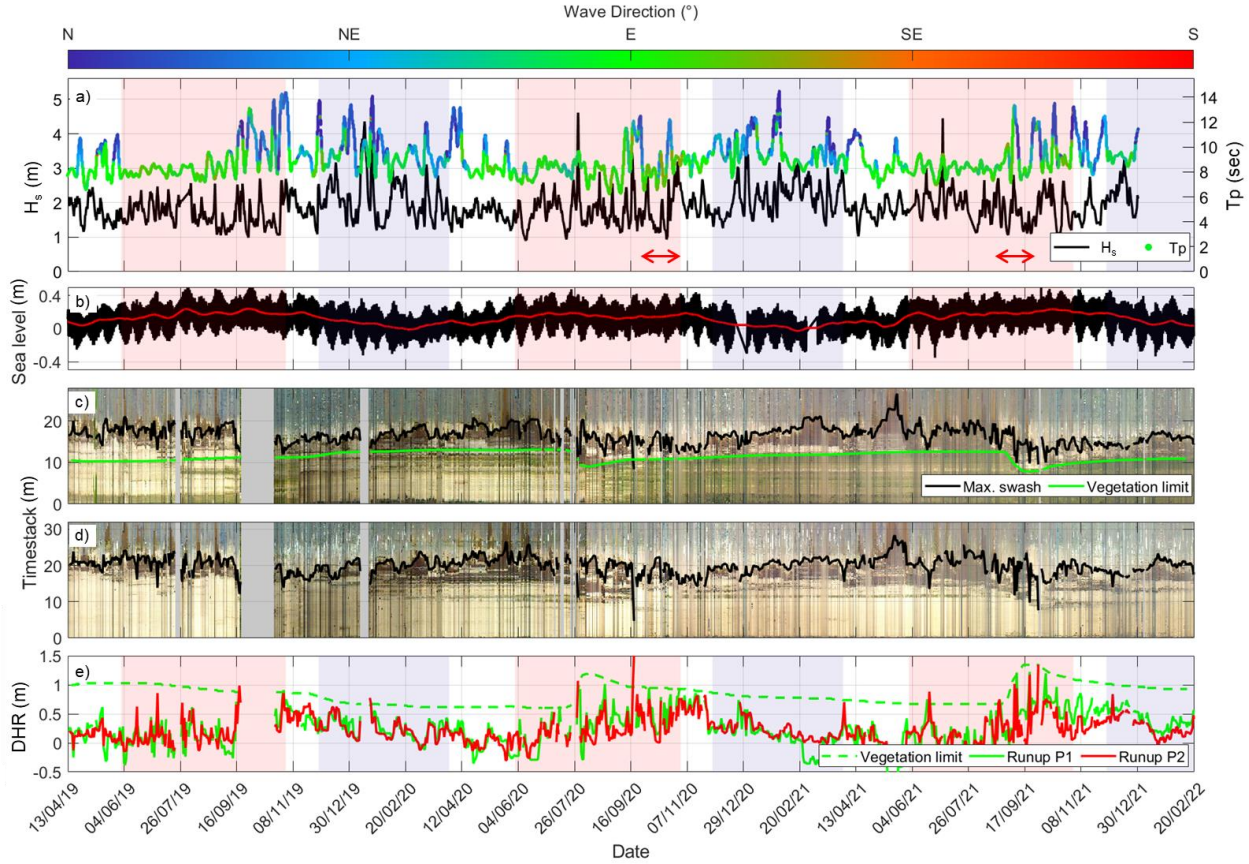

Figure 2. Camera derided observations and incident wave and sea-level conditions from April 2019 to May 2021. (a) Offshore significant wave height (H_s) and peak period (T_p) with associated, wave mean direction (Dp) is represented by the color of Tp points. Red arrows represent period of local hydrodynamic measurements campaign on site. (B) Sea-level variations on Pointe-à-Pitre tide gauge, 14 days moving mean is represented in red. (c) and (d) daily timestacks with detection of maximum swash limit (red line) and vegetation limit (green line) on P1 and P2 respectively. (e) Evolution of the DHR on both profile and vegetation limit height on P1. On every plots but timestacks winter are indicated by a blue background and cyclonic seasons by a red background.

						DHR (m)		Vegetation
Event id	Peak Date	Season	Hs (m)	Tp (sec)	Dp (°)	P1	P2	retreat (m)
1	17/09/2019	Cyclonic	2.5	12	15	0.7	0.7	-
2	29/10/2019	Cyclonic	2.6	14.6	40	0.9	0.9	-
3	17/12/2019	Winter	3.2	9.4	77	0.4	0.4	-
4	16/01/2020	Winter	4.4	10.8	54	0.7	0.8	-
5	08/02/2020	Winter	3.2	9.1	80	0.2	0.2	-
6	10/03/2020	Winter	3.1	13.7	354	0.1	0.1	-
7	29/07/2020	Cyclonic	4.6	11.1	76	1,0	1.1	-
8	17/09/2020	Cyclonic	3.4	10.8	110	1.4	1.5	3
9	29/10/2020	Cyclonic	3.1	9.3	78	0.8	0.8	-
10	01/01/2021	Winter	3.6	14.1	38	0.5	0.5	-
11	18/02/2021	Winter	3.2	9.3	76	0.1	0.1	-
12	18/03/2021	Winter	3	13.9	355	0.2	0.2	-
13	17/06/2021	Cyclonic	3	8.7	82	0.9	0.7	-
14	02/07/2021	Cyclonic	4.5	11.1	105	nd	nd	-
15	07/09/2021	Cyclonic	2.8	13.6	88	0.9	1.2	4
16	20/09/2021	Cyclonic	2.7	7.9	100	1.2	1.2	-
17	28/09/2021	Cyclonic	2.6	9.2	115	1.3	1.3	-
18	18/12/2021	Winter	3.3	9.8	61	0.6	0.5	-

Table 2. Storms observed during the study period. nd: no data.

In order to evaluate the relation between offshore conditions and local DHR a set of linear regressions was performed. The mean value of runup (0.5 m) and the elevation of vegetation limit (evolving from 0.6 to 1.1 m) are used to classify runup intensities. Figure 3 shows the linear correlation between the DHR extracted from cameras and offshore hydrodynamic parameters. Figure 3 (a), (b) and (c) represent offshore wave parameters from corrected MARC model (respectively H_s, Tp, and Dp) and Figure 3 (d) represent the correlation with the sea level measured at Pointe à Pitre tide gauge. Correlations with offshore wave conditions are weak with $R^2 < 0.3$, while correlation with the sea level is moderate $R^2 = 0.46$.

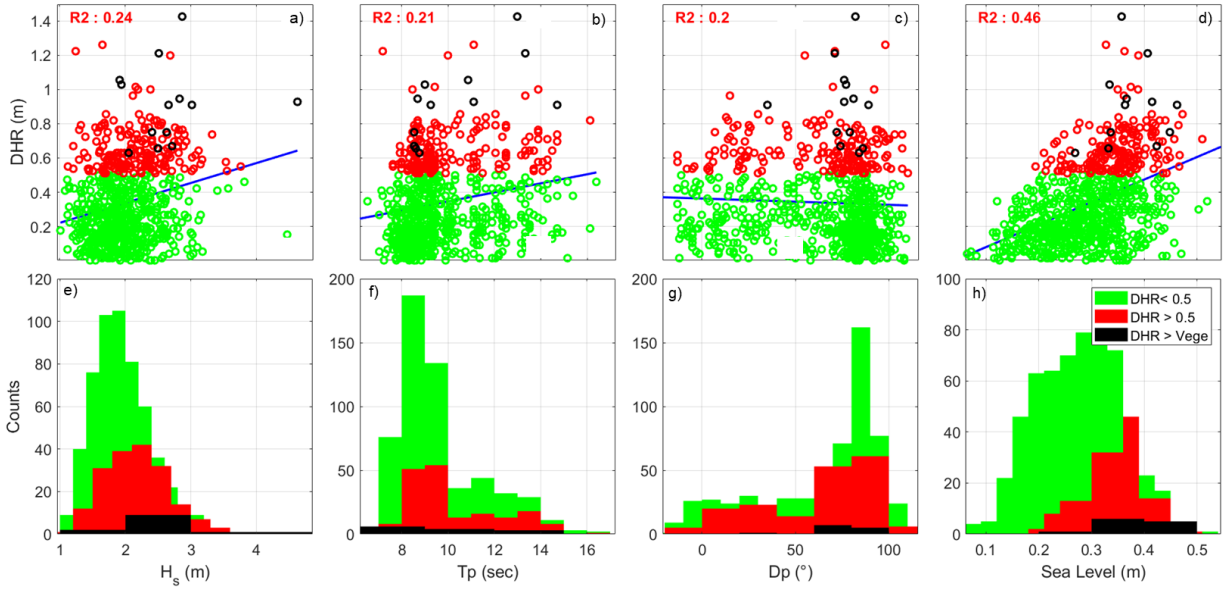

Figure 3. Linear regressions of DHR and (a) H_s, (b) Tp, (c) Dp and (d) sea level. (e), (f), (g) and (h) respective distribution histograms. Observations for runup less than 0.5 m are plotted in green, for runup greater than 0.5 m are plotted in red and runup exceeding the vegetation limit are plotted in black.

As the DHR dataset showed a great seasonal variability, a sinusoidal fitting was applied in order to highlight the annual cyclicity. The amplitude of the annual cycle (365.25 days/cycle) is estimated at 0.38 m, with a phase peak at day 307.5 (November 5th) with an R^2 of 0.48 with raw data, it represents 24% of the overall runup amplitude. In order to isolate the effect of sea level, storm periods were removed from the timeseries of DHR to suppress the effect of storm surges and unusual waves (see figure 4 (b)). Some extreme runup events remain visible in particular around September 17th 2021. This may be due to an underestimation of waves by corrected MARC Model, as the agitation is qualitatively validated by camera observations. The storm-filtered annual signal has a phase peak at day 250.5, an amplitude of 0.29 m and a R^2 of 0.52 with the storm filtered runup signal, thus very close to sea level annual component (phase peak at day 247.6 and amplitude of 0.2 m (Figure 4.(d)). Furthermore, when the annual sea level cycle is removed from the times series of the raw DHR, we obtained a runup signal that still shows an annual cyclicity with a phase of 335.5 days and 0.33 m amplitude. Figure 4 (e) presents the evolution and annual cyclicity of wave power ($H_{rms}^2 * T_p$) in m²/s. The signal obtained fluctuates greatly and is very chaotic. The calculated annual periodicity shows bad skills with raw data (R^2 = 0.24) suggesting a better correlation with another periodicity. Nevertheless, the phase is 333.5 days, which is very close to the sea level filtered runup signal.

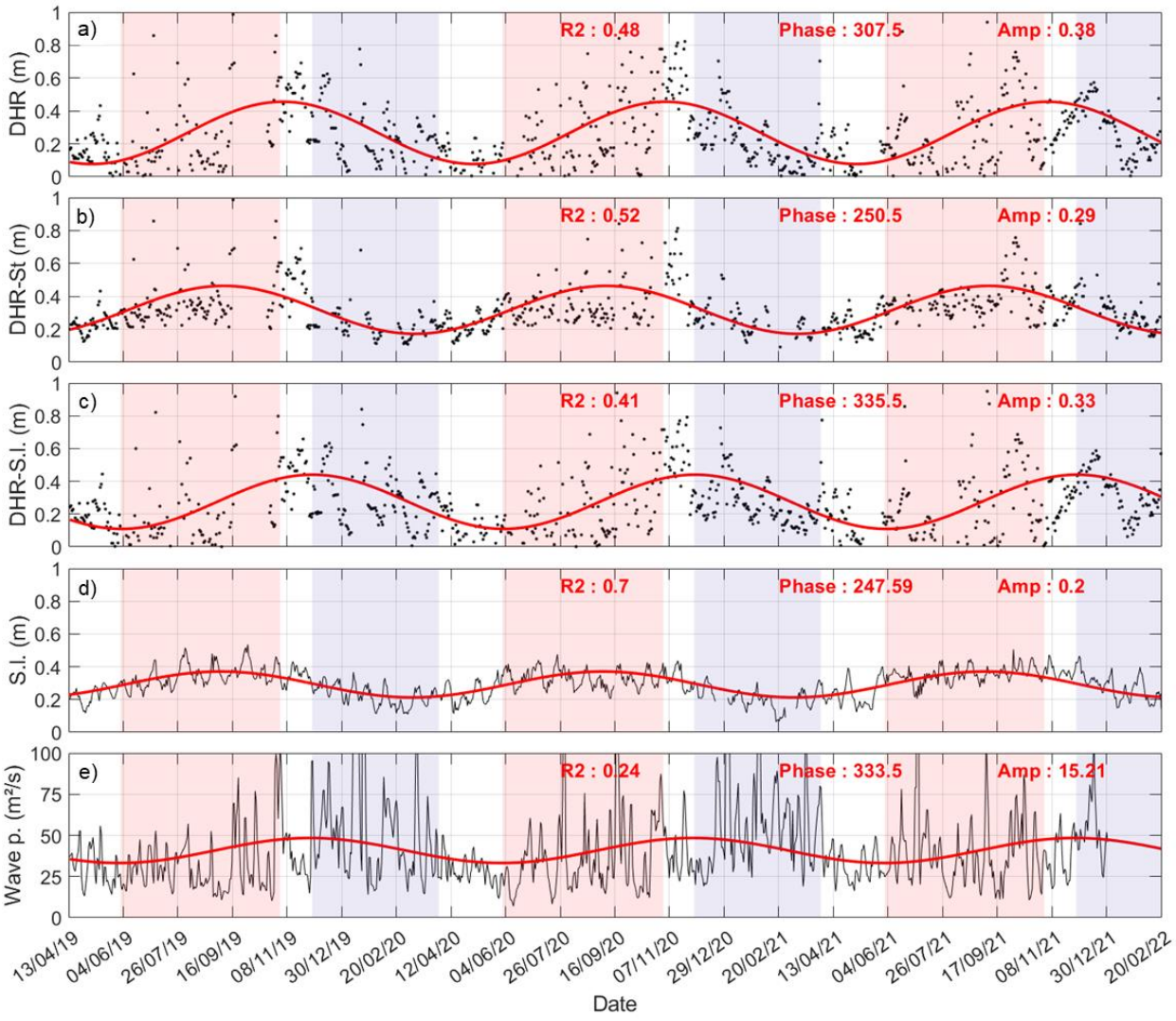

Figure 4. (a) Raw DHR observed on camera, (b) DHR with removal of storms periods, (c) DHR with removal of sea level annual periodicity, (d) Sea level with tide effect substracted, (e) Wave power. Runup observations are plotted in black points, sea level and wave power in black line and annual periodicity in red line.

These results indicate that the DHR signal presents a strong annual seasonality. When main storms period is removed from the signal, the periodicity calculated on the residual is in phase with the effect of sea level annual variability, suggesting a strong modulation of runup by sea level annual seasonality. At the opposite, when this sea level variability is removed from raw runup, a good correlation between the residual annual periodicity and swell annual periodicity appears which may indicate a swell modulation as well on the runup. This double dependency of sea level and wave climate annual cyclicity on runup induces a periodicity to the runup with a specific phase.

2.4 Mid/short-term observations

The data from onsite measurements were used to identify processes involved in nearshore hydrodynamic transformation by the reef. Figure 5 presents the hydrodynamic times series

during both campaigns including offshore conditions from corrected MARC model, sea level from Pointe à Pitre tide gauge. The 2020 campaign shows three energetic periods (offshore $H_s > 2$ m), for more information see events A, B and C on Table 3. Maximum offshore H_s reached 2.9 m on October 01st (event A) according to corrected MARC model outputs. The 2021 campaign shows 4 events above 2 m, events D, E, F, and G on Table 3. The maximum H_s is reached on September 07th (event F) with a value of 2.8 m. All these events remained moderate in terms of intensity and are related to cyclonic activity in the Atlantic basin relatively far from the study site. It is visible from the measurements in the reef flat that spectral transformation inshore is not constant over time. Indeed, periods of agitation show greater proportion of IG and VLF in the reef flat than during calm periods. A clear tidal modulation is also visible on SW band in the reef flat with greater values during high tides. On the 2021 campaign, the sensor at the North of the reef flat (NRF21, on Figure 1 (b)) shows slightly lower agitation but with the same dispersion than the reef flat sensor on the transect (RF21, on Figure 1 (b)). At the opposite, the sensor at the south of the reef flat (SRF21, on Figure 1 (b)) shows values close to the reef crest sensor. Thus, tidal modulation on SW is not visible and overall agitation is higher. Regarding H_{rms} transmission, percentages between the front reef and the reef flat (Figure 5 (e) and (f)) SW band wave height is always highly dissipated with transmission ranging from 10 to 60 %, on the other hand, SW and VLF band wave height are amplified at all time with transmission ranging from 115 to 300 % and 195 to 420 % respectively.

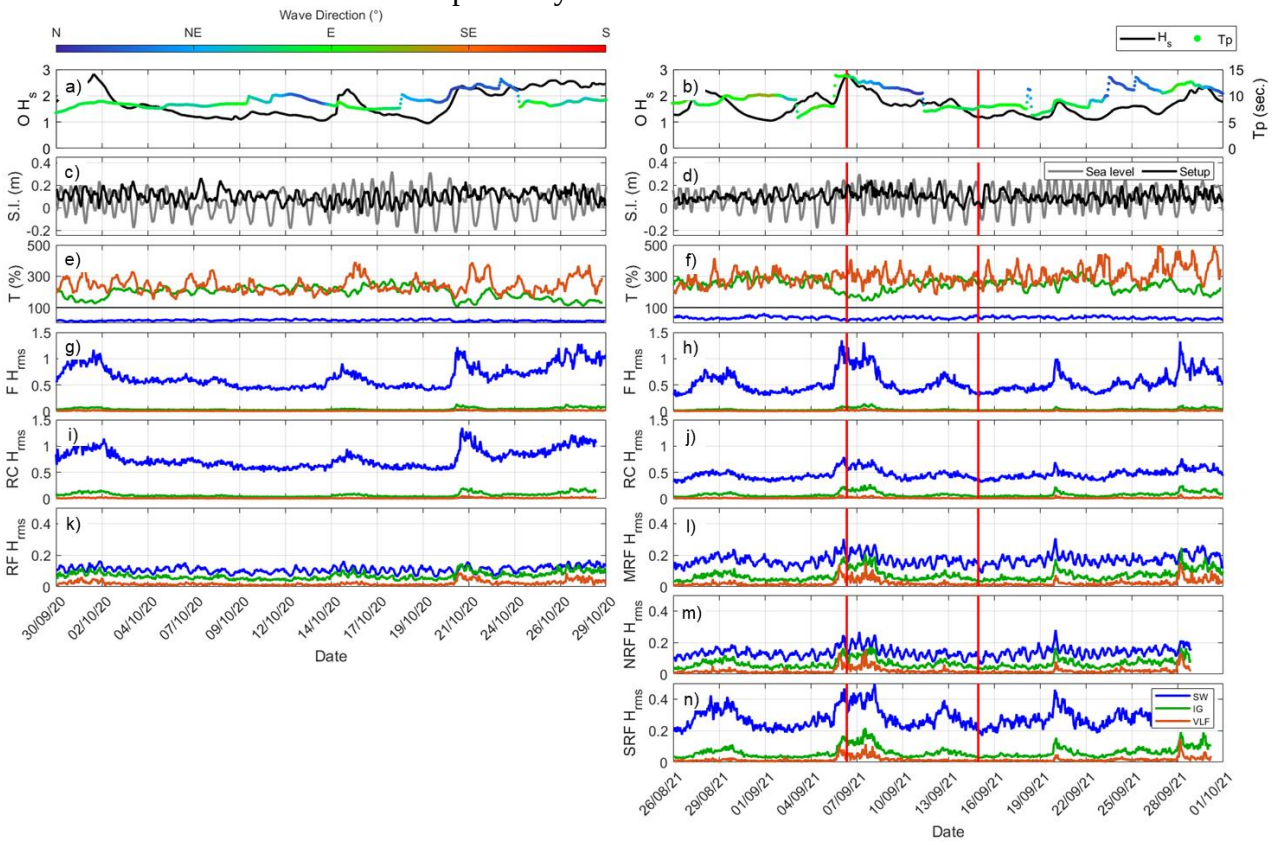

Figure 5. Left Column corresponds to hydrodynamic conditions for the 2020 campaign and right column corresponds to hydrodynamic conditions for 2021 campaign. (a-b) Offshore H_s , (c-d) sea level measured at Pointe-à-Pitre tide gauge setup from sensors, (e-f) H_{rms} transmission percentage according to spectral bands between the front reef and the reef flat , the horizontal

line is set at 100 % and represents a strict conservation of H_{rms}. H_{rms} chronic specifying SW (blue), IG (green) and VLF (orange) band for (g-h) front reef , (i-j) reef crest and (k-l) reef flat. H_{rms} evolution for sensors (m) at the North (n) at the South of the reef flat.

					DHR (m)	
Event id	Peak Date	Hs (m)	Tp (sec)	Dp (°)	P1	P2
A	01/10/2020	3.0	9.5	80	0.9	0.9
B	15/10/2020	2.1	7.5	90	0.6	0.7
C	29/10/2020	2.6	8.2	75	0.8	0.8
D	28/08/2021	2.2	9,0	95	0.2	0.3
E	07/09/2021	2.8	14.3	90	0.8	0.8
F	21/09/2021	1.9	9.6	90	1.2	1,0
G	28/09/2021	2.2	12.0	60	1.1	1.2

Table 3. Most agitated periods of 2020 and 2021 measurements campaigns

Figure 6.(a) presents mean H_{rms} value for each sensor. Sensors corresponding to a cross-shore transect are bounded by a line as on Figure 1. This figure gives an overview of H_{rms} evolution from the front reef to the reef flat compiling all sensors showing the specific behavior of each kind of waves while propagating onshore. A clear attenuation of SW band appears when comparing front reef and reef flat sensors. The sensor near reef crest for the 2020 campaign shows greater values than offshore which could be due to the wave shoaling occurring at this position. The reef crest sensor of 2021 campaign was positioned inshore, probably preventing to observe this amplification. IG band shows a maximum at reef crest position and then an attenuation in the reef flat and VLF band shows a progressive amplification from offshore to the reef flat. Comparing to the sensor in the reef flat on the cross-shore transect, sensors located on

either side of the reef flat show higher SW band mean H_{rms} but lower IG and VLF band H_{rms} for the southern sensor and lower mean H_{rms} values on all frequency bands for the northern sensor. Figure 6.(b) presents the mean spectra for the three sensors on the cross-shore profile of the 2021 campaign. The progressive attenuation of energy in the sea-swell band is noticeable as well as the amplification to the lower bands.

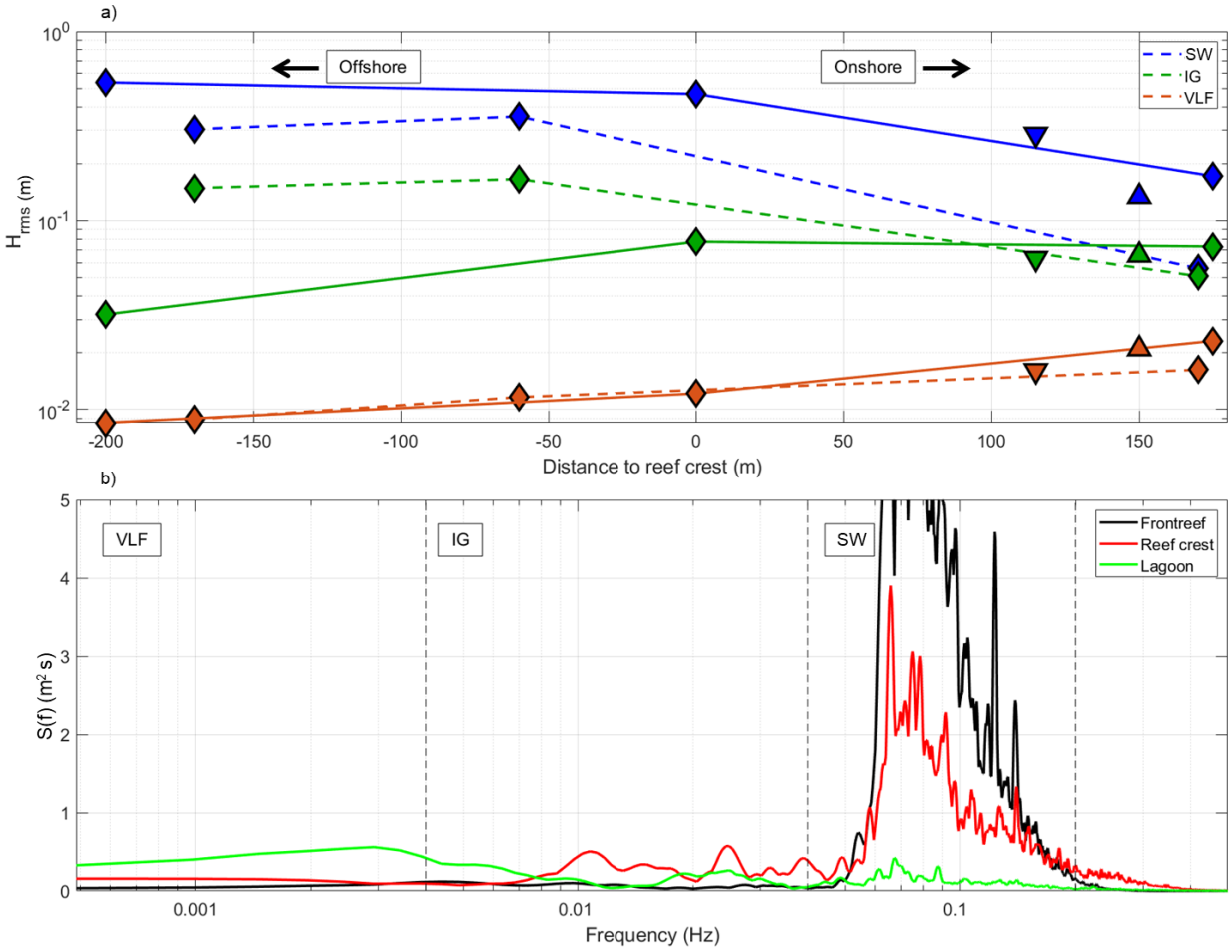

Figure 6. (a) Mean H_{rms} by sensor for the two campaigns. Sensors located on the same cross-shore transect are plotted with diamonds and linked by a line. Dotted line corresponds to 2020 campaign and solid line to 2021 campaign. Sensors disposed at the North and South of the reef flat for the 221 campaign are plotted with an upward triangle and a downward triangle respectively. SW band observations are plotted in blue, IG band in green and VLF band in brown. (b) Maximum wave spectrum for 2021 campaign. In order to facilitate observations on low frequency band, the Y-axis is in logarithmic scale.

The set of regressions performed on figure 7 compare incident conditions with hydrodynamic in the reef flat. Thus, it highlights relationships between offshore hydrodynamic (wave and sea-level variations) and reef-induced nearshore wave transformation.
The R^2 corresponds to the squared Pearson coefficient for all comparisons excepting those with Dp where the circular-linear correlation is applied. The correlation between SW band H_{rms} and offshore H_s is moderate in the reef flat (R^2 = 0.46) and strong for lower frequencies bands (R^2 =

466 0.72 and 0.6 for IG and VLF respectively). Furthermore, correlations between sea level and H_{rms}
467 in the reef flat show significant correlation for SW band primary but also for IG band but to a
468 lower extent (R^2 = 0.65 and 0.26 respectively). VLF band H_{rms} seems correlated with offshore
469 H_{rms} and Tp. The correlation with offshore Dp and H_{rms} remain relatively weak on each band
470 with R^2 values ranging from 0.11 to 0.24.
471

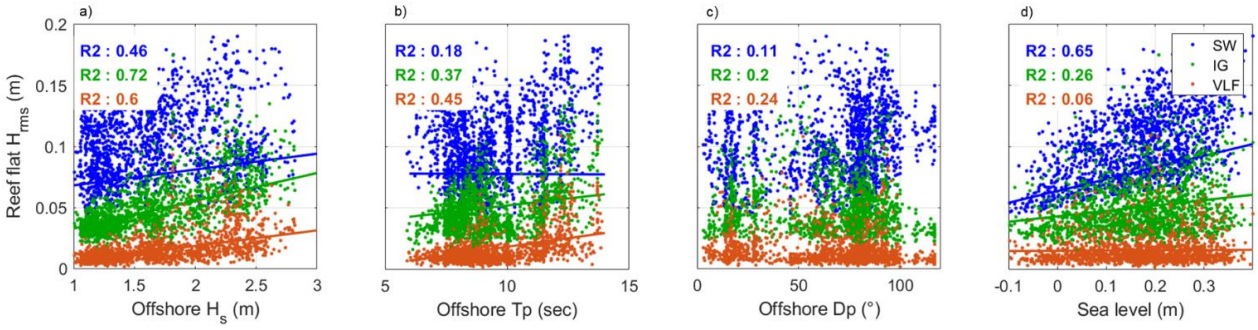

472

473 **Figure 7.** Linear regressions of H_{rms} measured at the reef flat against offshore wave parameters
474 (a) H_s, (b) Tp and (c) Dp and (d) sea level measured at Pointe-à-Pitre tide gauge.This figure
475 combines 2020 and 2021 hydrodynamic measurements.

476 Adequate conditions for low frequency development was further analyzed. IG and VLF wave
477 heights on the reef crest and in the reef flat were compared to concomitant front reef wave
478 conditions expressed here by wave power ($H_{rms}^2 * T_p$) in m²/s as in Sous et al., (2019) (Figure
479 8). Overall, a strong correlation between front reef wave power and H_{rms} is identified with better
480 skills on low frequency waves H_{rms} (R^2 ranging from 0.55 to 0.69) and in particular on the IG
481 band. The correlation in the latter remains constant through the reef while for the VLF the
482 correlation is greater in the reef flat (R^2 = 0.66 in the reef flat against 0.55 on the reef crest). We
483 note a significant correlation between IG band H_{rms} in the reef flat and sea level (R^2 = 0.29), such
484 correlation is not observed on the reef crest.
485

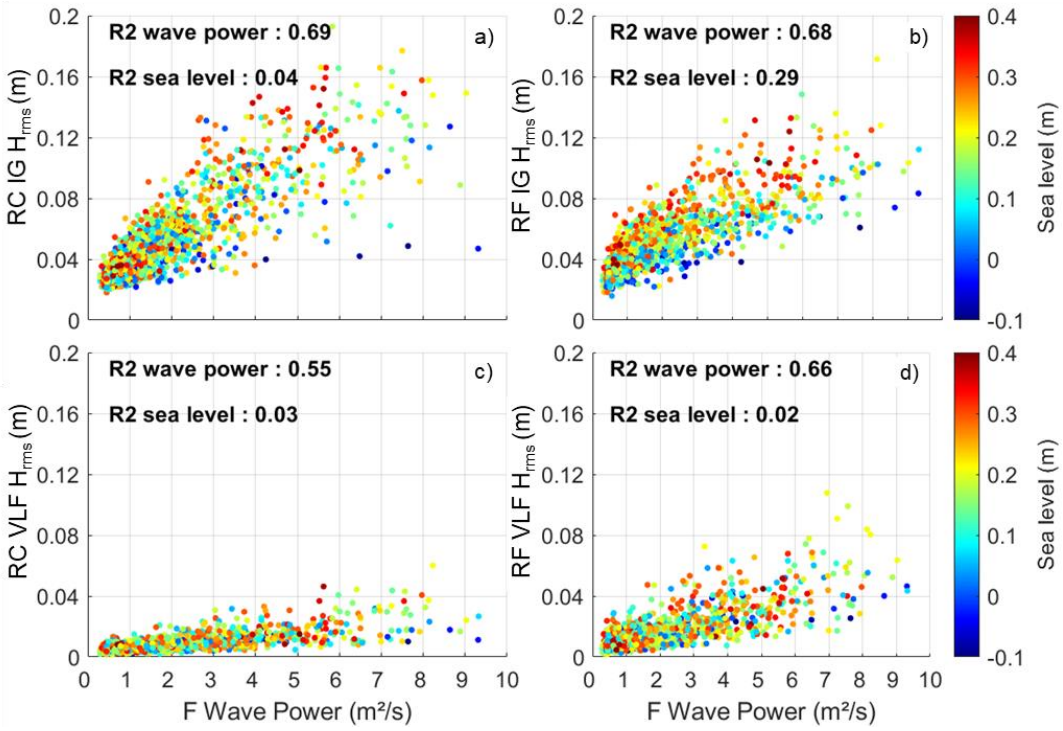

Figure 8. Front reef ("F") wave power against IG band H_{rms} (upper row) and VLF band H_{rms} (lower row) on the reef crest ("R", left column) and in the reef flat ("RF", right column). The color represents sea-level variations.

In order to identify the relative implication of different composants of the agitation in the reef flat on the runup, observations in the reef flat were associated with DHR extracted from cameras for 2020 and 2021 campaign (Figure 9). The higher magnitude events observed on figure 8 appears clearly on the runup time series. Periods of particularly low runup are also identified from September 07th to 11th 2020, from August 31th to September 5th and from September 11th to September 18th 2021 and appears uncorrelated from local agitation. A visual check on images indicates that those periods correspond to massive sargassum arrivals, which tends to disappear from the reef system when the agitation gets greater. Excluding sargassum beaching periods, DHR seems strongly correlated with agitation in the reef flat; the visual correlation is particularly marked on 2021 campaign.

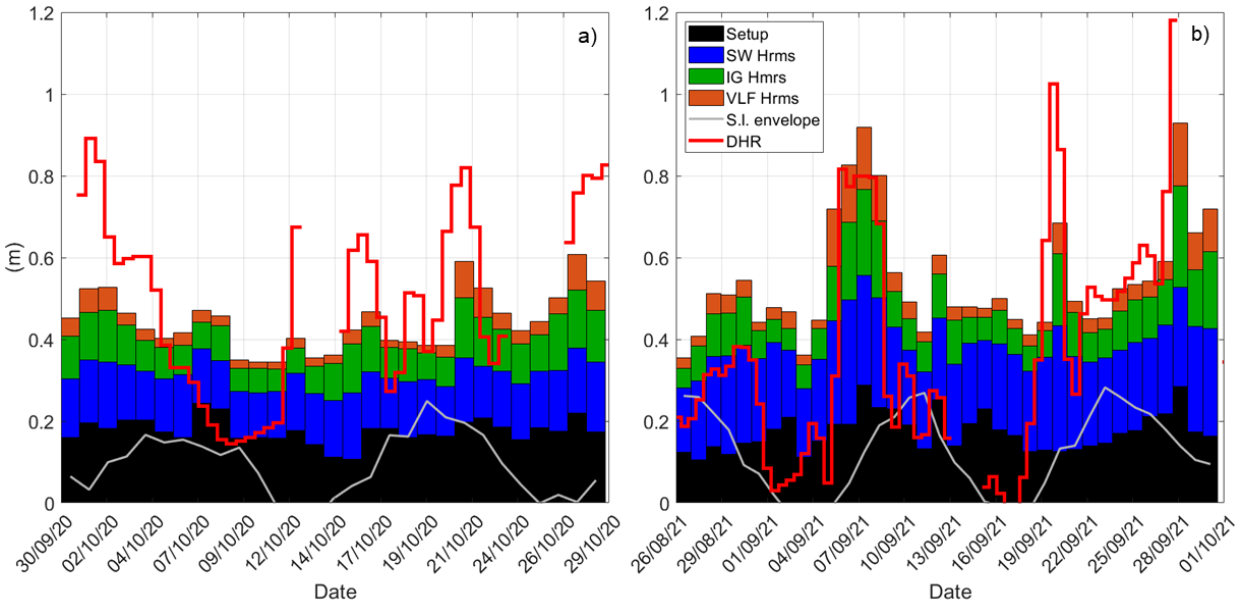

Figure 9. Hydrodynamic measurements in the reef flat (a) 2020, (b) 2021 represented by stacked bar plot with setup in black, SW band H_{rms} in blue, IG band H_{rms} in green and VLF band H_{rms} in brown. Sea-level envelope is plotted in gray and DHR from the camera in red.

A new set of regressions was performed in order to quantify observations from Figure 9 coupling DHR and hydrodynamics in the reef flat. As an unique value per day is extracted for runup, it would be inadequate to compare here runup with sea level signal including tidal semi-diurnal variations. Therefore, the daily envelope was extracted and used for the regression. Figure 9 presents the result from the linear regressions.

A significant agreement with H_{rms} on every frequency band is identified with better results on lower frequency band (R^2 = 0.62 and 0.52 for IG and VLF band) than on SW band (R^2 = 0.45). Correlation with sea-level envelope is lower (R^2 = 0.39) and the correlation with setup is the lowest (R^2 = 0.28).

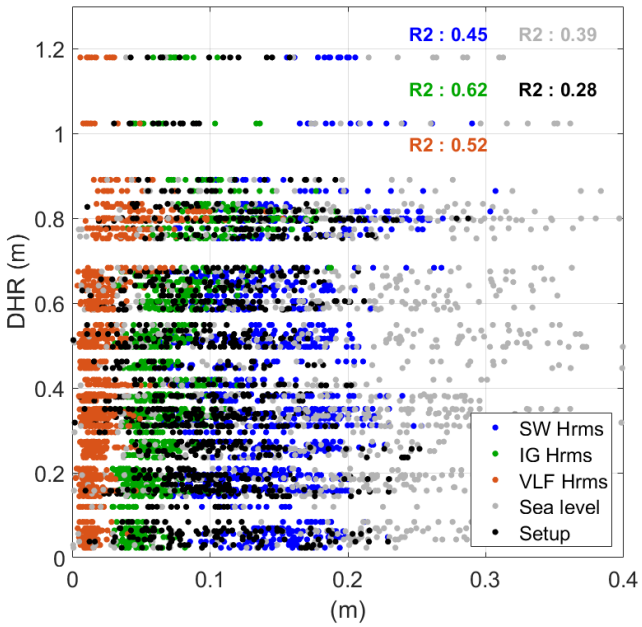

Figure 10. Linear regression of SW band H_{rms}, IG band H_{rms}, VLF band H_{rms}, sea-level envelope and setup from measurements in the reef flat position for 2020 and 2021 campaigns against DHR from cameras.

Results from field measurements show a high correlation of offshore overall agitation with IG and VLF intensity. When comparing processes measured in the reef flat with DHR from camera observations, a strong correlation with lower frequency bands is noted. The difference in sampling frequency between runup from the camera and on-site hydrodynamic measurements limits the comparison at a finer scale.
IG and VLF development is highly dependent of the incident wave power in particular for IG band. The attenuation visible in the reef flat suggests a dissipation on the reef crest and an attenuation on the reef flat modulated by sea level. VLF components are well correlated to front reef wave, which may indicate a development in the reef flat from SW, or IG band waves.

3 Discussion

In this study, a continuous multi-year runup time series obtained by video monitoring is used in combination with offshore wave datasets and local hydrodynamic measurements in a fringing reef system. This allows further analyses at different times and spatial scales of the key processes and parameters involved in the control of the runup.

3.1 Event scale processes

Wave transformation observations through the fringing reef from the sensor data installed on site shows that overall wave energy is highly dissipated (overall mean attenuation of 65%). As described in many previous studies, most of the attenuation occurs on the reef crest, which is the location of wave shoaling and breaking (e.g., Lowe et al., 2005). The spectral analysis, allowing the split of the whole spectra into a SW band, an IG band and a VLF band, indicates very different behaviors between spectral bands. Indeed, only the short waves which represent the vast majority of offshore spectra energy are subject to attenuation. IG band shows a net amplification on the reef crest followed by a slight/moderate attenuation when reaching the

shoreline. This is visible from the slight reduction of IG undulations observed on the reef flat sensors comparatively to the reef crest sensor. This attenuation is sea level dependent as lower IG waves are observed for the same offshore conditions but for low tide levels. A similar correlation with a stronger dependency was measured for SW waves in the reef flat. On the other hand, VLF show a greater amplification in the reef flat suggesting a transmission of energy on the reef crest from short waves to IG waves and progressively in the reef flat from IG waves to VLF waves. At the opposite of IG waves, no correlation with sea level is noted in the amplification. Figure 11 illustrates this by giving snapshots comparing waves spectral transformation firstly during a storm at high and low tide and secondly during calm period also at high and low tide. The energy switch from SW band to IG/VLF band is particularly important at high tide and less marked at low tide. Furthermore, the amplification of IG on the reef crest is followed by an amplification on late IG/early VLF band in the reef flat.

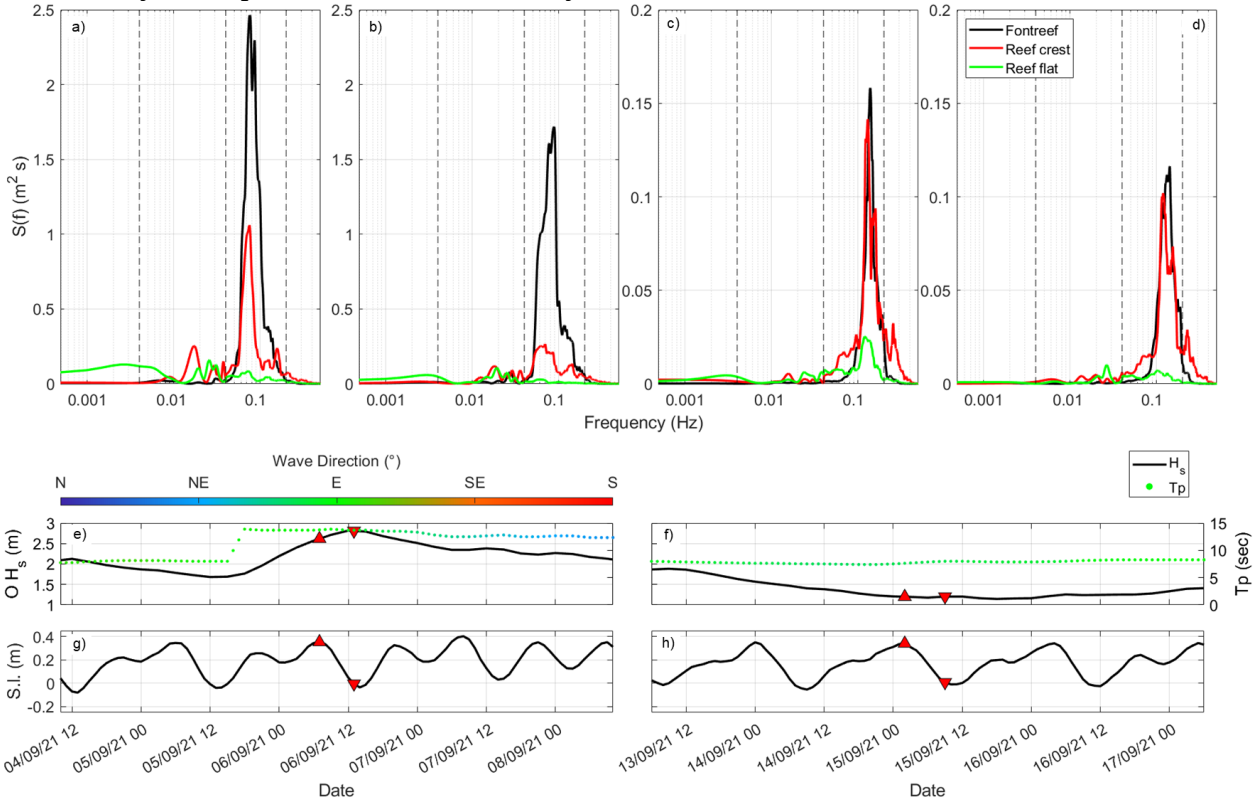

Figure 11. Energy spectras at front reef position (black line), reef crest (red line) and reef flat position (green line) corresponding to storm conditions on September 06th at high (a) and low (b) tides and calm conditions on September 15th at high (c) and low (d) tides. Offshore wave conditions (e and f) and sea-level variations (g and h) are plotted under spectral graphs for both periods. The period of the extracted bursts is represented by an upward red triangle for high tide and downward red triangle for low tide.

3.2 Seasonal scale processes

Our results show a strong seasonal control on runup maximum elevation. However, this seasonality appears to be different from the seasonal oscillations of the water level, and from the seasonal variations of sea state in phase and amplitude. By retrieving sea-level seasonality from raw runup dataset, one finds the wave runup signal with a phase very close to sea state seasonality and vice

versa. Wave climate periodicity is generated by both events mostly clustered on particular periods (winter and cyclonic seasons) and residual agitation (greater during winter) (Reguero et al., 2013). This cycle has an impact on runup periodicity as a similar pattern is found on runup signal with sea-level effect filtered. The effect of both cycles leads to an annual periodicity on DHR with its own phase with minimas in May and maximas in November.

In the context of Caribbean Islands and for the period of the study (3 years), among all processes involved in sea level variations, only the steric effect (Torres and Tsimplis, 2012) seems to be a good candidate to explain the seasonal DHR variability. Indeed, steric effect in this part of the Caribbean was reported to influence sea level about approximately 15 cm at seasonal time scale (Torres and Tsimplis, 2012). However, the direct effect of this periodicity on oscillation at shoreline level and the implication on coastal flooding has been rarely discussed (Rueda et al., 2019). Only a few studies focused on continental Caribbean beaches (without reef ecosystem) report an impact of such variation son coastal inundation (Orejarena-Rondón et al., 2019; Genes et al., 2021). Annual variability of wave climate is also known in the Caribbean (Reguero et al., 2013). Nevertheless, its impact on runup on reef line-coast had not been identified so far. Our results indicate that the effect of seasonal sea-level variation on DHR and swash excursion is significant. This periodicity present an amplitude of 0.37 m which represents 24% of the overall runup variability. During the low phase of the annual variability, which occurs in May, the effect of storms on runup is attenuated and during the high phase (peak) of the annual cycle occurring in October, storms of mild intensity may generate unexpected runup. Furthermore, a greater portion of incident energy reaches the shoreline level during the amplifying portion of the annual cycle and it is visible on figure 2 (c) and (d), which has an impact on shoreline morphology. In other words, this annual variation may be responsible for seasonal shoreline migration and beach morphologic evolution not directly attributable to wave forcing. This corroborates other shoreline observations from video system on reef-lined beach in Guadeloupe (Moisan et al., 2021).

3.3. Coral reef implication

During a random storm, runup will present tidally controlled variations within the event (Figure 11), and the occurrence of the event within the annual periodicity will induce an overall mitigation or amplification of the runup (Figure 4). These processes, comprising astronomic tide, steric expansion annual periodicity and wave climate, act on water depth and consequently on reef submergence. Coral reef wave filtering by wave breaking and bottom friction are dependent on water depth above the reef. Low water depth on the reef induces a high filtering of the swell while high water depth induces a lower filtering and a greater wave energy potentially reaching the beach. Such phenomenon is also observed on sandy beaches with sedimentary or rocky structures like bars (e.g., Melito et al., 2022) but it is amplified in the presence of a coral reef in consequence of the steepness, the potentially wide width of the coral platform, the high structural complexity and crest shallowness of such an environment. Overall, the wave transformation observed from the front reef to the reef flat reflects a shift from high to low frequencies leading to IG waves of the same order of magnitude as the SW as it approaches the coastline in particular during storms (up to 0.2 m on each frequency band), whereas these low-frequency undulations were almost insignificant before reaching the reef level (Figure 7). This result indicates that most IG and VLF are generated by breakpoint forcing (Symonds et al., 1982) and a minor fraction come from incident bound long waves (Longuet-Higgins & Stewart, 1964). This corroborates hydrodynamic observations commonly made on coral reefs environments (e.g., Péquignet et al., 2009; Pomeroy et al., 2012; Cheriton et al., 2016; Masselink et al., 2019). By quantifying

dissipation/amplification of the incident wave through the reef, we measured a difference on transmission between calm and agitated conditions. Indeed, the transmission in IG band from the front reef to the reef flat is inversely proportional to offshore wave conditions, thus a greater proportion of SW band waves must be transferred into IG band during calm conditions than during stormy conditions (although IG wave amplitude is positively correlated with offshore wave power as shown figure 7 (c) and (d)). As the transmission percentage also decreases with offshore agitation on the SS band and as VLF band waves transmission does not show correlation with front reef wave power (figure 12 (c), (d) and (e), we assume that a greater portion of incident waves is simply dissipated for storm conditions. Here, the generation and behavior of VLF band waves is poorly associated with parameters other than offshore wave power, which may be due to the chaotic aspect of the reef and the restricted dimensions of the site which could limit the generation of such undulations (Cheriton et al., 2020). It is also why overall mean wave energy dampening is approximately 65% while it can reach more than 90% on wider and continuous reefs (Harris et al., 2018). Thus, a majority of incident wave energy mainly carried by SW band waves is dissipated on the reef crest, a proportion of those incident SW band waves is transformed into IG band waves, again a proportion of those IG waves is transferred to VLF band waves in the reef flat.

Furthermore, additional sensors placed on either side of the transect in 2021 helped in understanding of the local longshore variability (Figure 12). The sensors installed at the South of the reef flat show the greater agitation in particular on SW band (H_{rms} up to 0.5 m during storm event and a mean transmission of 55.5%) and no tidal mitigation on H_{rms} at all frequency bands. This reflects the poor wave filtering by the reef at this cross-shore location as its structure is sparser (narrower overall) and deeper here. At the opposite, the sensors installed at the North of the system show a greater attenuation on the SW band and similar agitation on the IG and VLF band (SW band H_{rms} up to 0.23 m and a mean transmission of 27.9%). At this cross-shore location, the reef offers a continuous shallow barrier and the reef flat is shallower as well. This implies that the absence of the coral reef or a degraded version of the actual reef in width and crest shallowness would lead to less control on the agitation in the reef flat and hence an increase in runup. This confirms previous results observed or modeled on other studies stating that depth over reef and reef width are the main reef intrinsic parameters involved in backreef agitation (Cheriton et al., 2020) and runup (Pearson et al., 2017). This also supports the importance of living reef as a healthy coral ecosystem maintains a constant depth overtime while rocky structures constituted of dead colonies tend to erode. This latter point is in particularly significant in the actual context of sea level rise (Perry et al., 2018).

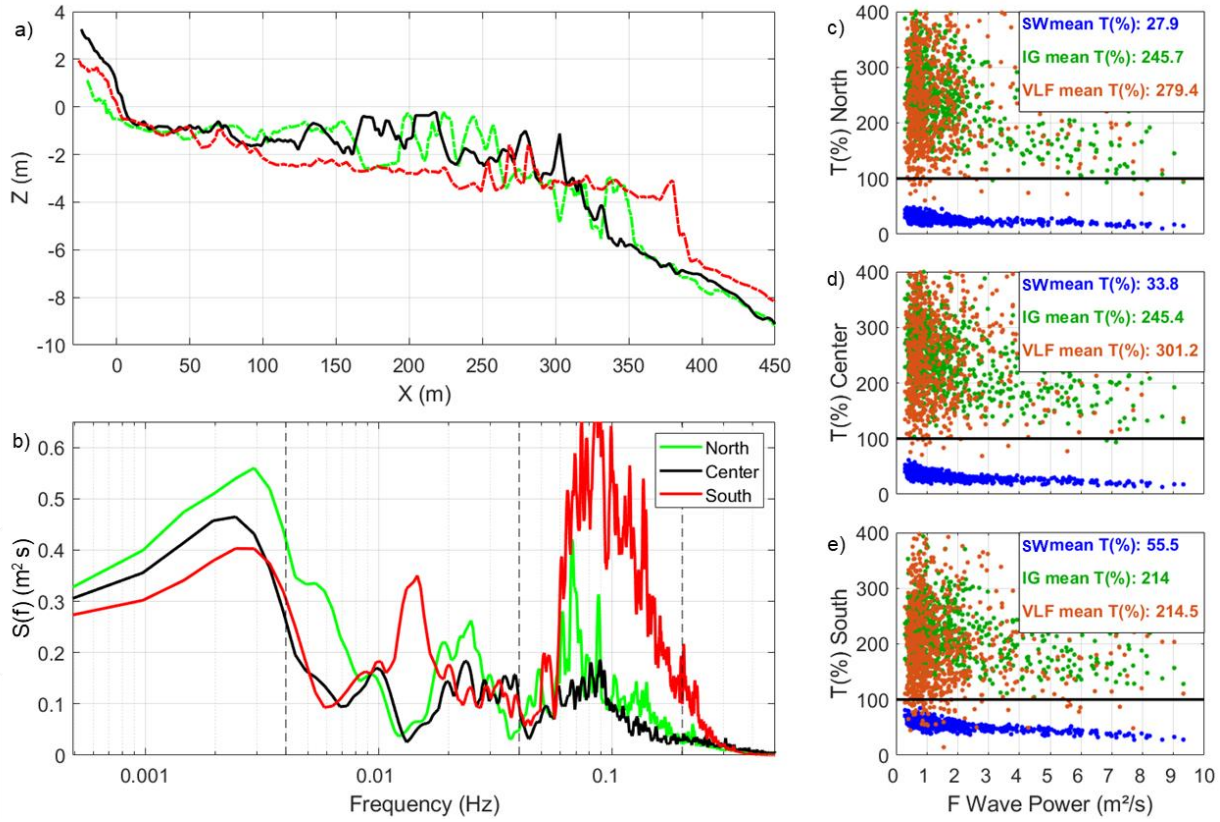

Figure 12. (a) Cross-shore profiles and (b) max spectrum corresponding to the three pressure sensors installed in the reef flat for the 2021 campaign (see locations on Figure 1 (b)). Data corresponding to North position are plotted in green, Center position in black and South position in red. H_{rms} transmission on SW, IG and VLF band from front reef sensor to (c) North reef flat, (d) Center reef flat and (e) South reef flat.

Finally, the comparison of two profiles, one with and without upperbeach vegetation, showed a clear attenuation of runup by the vegetation during most extreme storm events (Figure 2 (c), (d) and (e). Pre-storm levels show equivalence between vegetated and non-vegetated profiles, but a gap is systematically observed between the profiles when the swash reaches vegetation limit. Events exceeding vegetation limit are rare on the study period but this dataset give promising indications that will need to be further analyzed.

5 Conclusions

For several years now, reef coastlines have been the object of increasing attention, with a particular focus on the hydrodynamic processes likely to generate coastal flooding, evidencing the dominant role of wave transformation over the reef. Using a ~3 years video monitoring of wave run-up, as well as measurements of waves dynamics and water levels on the fringing coral reef of Anse Maurice in Guadeloupe island, we analysed processes involved in swash inundation from event scale to seasonal scale.

Sensor datasets highlighted the role of incident wave conditions on IG and VLF band wave generation along the reef platform. The control on agitation in the reef flat by sea level was also identified with more filtering of the SW and IG band waves in the reef flat at low tide.

A strong annual periodicity was detected on camera-derived DHR and appears to be linked to sea level annual variations generated by steric effect and with annual variations of wave climate. Spatial differences in runup during storms were also noticed due to upperbeach vegetation. However, more research is needed to investigate the role of these ecosystem on reducing wave runup and thus coastal inundation, particularly during more extreme events.
In a changing climate with sea-level rise and a possible increase of extreme events, the higher submergence of reefs should induce an increase of runup and overwash events and reef coastlines to become more and more vulnerable. Obviously, our dataset is far too short to evaluate the effect of inter-annual oscillations (ENSO, NAO, etc.) or the effect of a rising sea-level. However, this quite long timeseries of daily maximum runup provides the scientific community with an unprecedented dataset for the validation of models to simulate more extreme events or for an analysis of the effects of climate change on these environments. In the continuity of this study, such a numerical experiment is being realized to study the processes during more intense storms than those observed during the study period.

Acknowledgments

The study takes part of a PhD thesis work funded by the BRGM within the EU Interreg Caribbean CARIB-COAST project budget. Offshore wave conditions extracted from MARC model were provided by the Ifremer. Tide gauge sea level observations were provided by the SHOM. The authors also thank T. Delahaye and M. Norden for their help in field experiments.

References

Aarninkhof, S.G.J. and Ruessink, B.G. (2004). Video observations and model predictions of depth-induced wave dissipation, in IEEE *Transactions on Geoscience and Remote Sensing, vol. 42*, no. 11, pp. 2612-2622, Nov. 2004, doi: 10.1109/TGRS.2004.835349

Almar, R., Bonneton, P., Senechal, N. and Roelvink, D. (2008). Wave celerity from video imaging: a new method. *Coastal Engineering*, pp. 661-673. doi: 10.1142/9789814277426_0056

Andriolo, U., Sánchez-García, E., Taborda, R. (2019). Operational use of Surfcam online streaming images for coastal morphodynamic studies. *Remote Sensing, 11*, 78. doi: 10.3390/rs11010078

Beck, M.W., Losada, I.J., Menéndez, P., Reguero, B.G., Díaz-Simal, P., Fernandez, F. (2018). The global flood protection savings provided by coral reefs. *Nat Commun 9*, 2186. doi: 10.1038/s41467-018-04568-z

Bergsma, E.W.J., and Almar, R., (2018). Video-based depth inversion techniques, a method comparison with synthetic cases. *Coastal Eng., 138*, 199–209, doi: 10.1016/j.coastaleng.2018.04.025

Bertin, X., de Bakker, A., van Dongeren, A., Coco, G., André, G., Ardhuin, F., Bonneton, P., Bouchette, F., Castelle, B., Crawford, W.C., Davidson, M., Deen, M., Dodet, G., Guérin, T., Inch, K., , Leckler, F., McCall, R., Muller, H., Olabarrieta, M., Roelvink, D., Ruessink, G., Sous, D., Stutzmann, E., Tissier, M., (2018). Infragravity waves: From driving mechanisms to impacts. *Earth-Science Reviews, Volume 177*, Pages 774-799, ISSN 0012-8252, https://doi.org/10.1016/j.earscirev.2018.01.002

Buckley, M. L., Lowe, R. J., Hansen, J. E., van Dongeren, A. R., and Storlazzi, C. D., (2018). Mechanisms of wave−driven water level variability on reef−fringed coastlines. *Journal of Geophysical Research, 123*, 3811–3831. doi: 10.1029/2018JC013933

Castelle, B., V. Marieu, S. Bujan, K. D. Splinter, A. Robinet, N. Sénéchal, and S. Ferreira, (2015). Impact of the winter 2013-2014 series of severe Western Europe storms on a double-barred sandy coast: Beach and dune erosion and megacusp embayments, *Geomorphology*, *238*, 135– 148

CEREMA, 2021. Fiches synthétiques de mesure des états de mer - Tome 3 – Outre-mer - Janvier 2021. Collection : Données. ISBN : 978-2-37180-499-9

Chadee, X.T., Clarke, R.M., (2015). Daily near-surface large-scale atmospheric circulation patterns over the wider Caribbean. Clim Dyn 44, 2927–2946. https://doi.org/10.1007/s00382-015-2621-2

Charles, E., Idier, D., Delecluse, P., Déqué, M., Le Cozannet, G., (2012). Climate change impact on waves in the Bay of Biscay, France. Ocean Dynamics 62, 831–848. https://doi.org/10.1007/s10236-012-0534-8

Chelton, D. B., and Enfield, D. B., (1986). Ocean signals in tide gauge records, *Journal of Geophysical Research*, *91*(B9), 9081– 9098, doi:10.1029/JB091iB09p09081

Cheriton, O.M., Storlazzi, C.D., Rosenberger, K.J., (2016). Observations of wave transformation over a fringing coral reef and the importance of low-frequency waves and offshore water levels to runup, overwash, and coastal flooding. *Journal of Geophysical Research: Oceans, 121* (5), 3121–3140. doi: 10.1002/2015JC011231

Cheriton O.M., Storlazzi C.D. and Rosenberger K.J., (2020). In situ Observations of Wave Transformation and Infragravity Bore Development Across Reef Flats of Varying Geomorphology. *Front. Mar. Sci. 7*:351. doi: 10.3389/fmars.2020.00351

Costa, M., Araújo, M., Araújo, T., Siegle, E., (2016). Influence of reef geometry on wave attenuation on a Brazilian coral reef, *Geomorphology*, *Volume 253*, Pages 318-327, ISSN 0169-555X, https://doi.org/10.1016/j.geomorph.2015.11.001

Ellison, J.C. (2018). Pacific Island Beaches: Values, Threats and Rehabilitation. In: Botero, C., Cervantes, O., Finkl, C. (eds) Beach Management Tools - Concepts, Methodologies and Case Studies. *Coastal Research Library*, *vol 24*. Springer, Cham. https://doi.org/10.1007/978-3-319-58304-4_34

Escudero, M. Mendoza, E. Silva, R., (2020). From Nature-Based to Ecologically Enhanced Beach Protection Strategies: an Experimental Comparison. 10.18451/978-3-939230-64-9_098

Ferrario, F., Beck, M.W., Storlazzi, C.D., Micheli, F., Shepard, C.C., Airoldi, L. (2014). The effectiveness of coral reefs for coastal hazard risk reduction and adaptation. *Nat. Commun. 5*, Article number: 3794. doi: 10.1038/ncomms4794

Fisher, R.A. (1958). Statistical Methods for Research Workers, *13th Ed., Hafner*.

Gawehn, M., van Dongeren, A., van Rooijen, A., Storlazzi, C. D., Cheriton, O. M., & Reniers, A. (2016). Identification and classification of very low frequency waves on a coral reef flat. *Journal ofGeophysical Research: Oceans*, *121*, 7560–7574. https://doi.org/10.1002/2016JC011834

Genes, L.S., Montoya, R.D., Osorio, A.F., (2021). Costal sea level variability and extreme events in Moñitos, Cordoba, Colombian Caribbean Sea, *Continental Shelf Research, Volume 228*, 104489, ISSN 0278-4343, https://doi.org/10.1016/j.csr.2021.104489

753 Guannel, G., Arkema, K., Ruggiero, P., Verutes, G. (2016). The Power of Three: Coral Reefs,
754 Seagrasses and Mangroves Protect Coastal Regions and Increase Their Resilience. *PLoS*
755 *ONE 11*(7): e0158094. doi:10.1371/journal.pone.0158094
756 Guillen, L. ; Pallardy, M., Legendre, Y., De La Torre, Y. ; Loireau.,C., (2017). -
757 Morphodynamique du littoral Guadeloupéen. Phase 1 : Définition et mise en place d'un
758 réseau d'observation et de suivi du trait de côte : Evaluation historique du trait de côte
759 Guadeloupéen. Rapport final. BRGM/RP-66653-FR, 109 p., 21 ann.
760 Harris, D. L., Rovere, A., Casella, E., Power, H., Canavesio, R., Collin, A., Pomeroy A., Webster
761 J.M., Parravicini V., (2018). Coral reef structural complexity provides important coastal
762 protection from waves under rising sea levels. *Sci. Adv. 4*:eaao4350. doi: 10.1126/sciadv.
763 aao4350
764 Holland, K.T., Holman, R.A., Lippmann, T.C., Stanley, J., Plant, N., (1997). Practical use of
765 video imagery in nearshore oceanographic field studies. *IEEE Journal of Oceanic*
766 *Engineering 22* (1), 81–92. doi: 10.1109/48.557542
767 Holman, R.A., Stanley, J., (2007). The history and technical capabilities of Argus. *Coastal*
768 *Engineering 54* (6–7), 477–491. doi: 10.1016/j.coastaleng.2007.01.003
769 Johnston, E., Ellison, J.C., (2014). Evaluation of beach rehabilitation success, Turners Beach,
770 Tasmania. *J Coast Conserv 18*, 617–629. https://doi.org/10.1007/s11852-014-0334-z
771 Knutson, T., Camargo, S. J., Chan, J. C. L., Emanuel, K., Ho, C., Kossin, J., Mohapatra, M.,
772 Satoh, M., Sugi, M., Walsh, K., and Wu, L. (2020). Tropical Cyclones and Climate Change
773 Assessment: Part II: Projected Response to Anthropogenic Warming. *Bulletin of the*
774 *American Meteorological Society 101*, 3, E303-E322, available from:
775 https://doi.org/10.1175/BAMS-D-18-0194.1
776 Le Cozannet, G., Idier, D., de Michele, M., Legendre, Y., Moisan, M. Pedreros, R. Thieblemont,
777 R. Spada, G. Raucoules, D. De La Torre, Y., (2020). Timescales of emergence of chronic
778 nuisance flooding in the major economic centre of Guadeloupe. 10.5194/nhess-2020-178
779 Longuet-Higgins, M. S., & Stewart, R. W. (1964). Radiation stresses in water waves; a physical
780 discussion, with applications. *Deep Sea Research and Oceanographic Abstracts, 11* (4),
781 529–562. doi: 10.1016/0011-7471(64)90001-4
782 Losada, I.J., Reguero, B.G., Méndez, F.J., Castanedo, S., Abascal, A.J, Mínguez, R., (2013).
783 Long-term changes in sea-level components in Latin America and the Caribbean. *Global*
784 *and Planetary Change, Volume 104*, Pages 34-50, ISSN 0921-8181,
785 https://doi.org/10.1016/j.gloplacha.2013.02.006
786 Lowe, R. J., J. L. Falter, M. D. Bandet, G. Pawlak, M. J. Atkinson, S. G. Monismith, Koseff,
787 J.R., (2005). Spectral wave dissipation over a barrier reef, *Journal of Geophysical*
788 *Research, 110*, C04001, doi:10.1029/2004JC002711
789 Lugo-Fernández, A., H. H. Roberts, and J. N. Suhayda, (1998). Wave transformations across a
790 Caribbean fringing-barrier Coral Reef, *Cont. ShelfRes., 18*(10), 1099–1124,
791 doi:10.1016/S0278-4343(97)00020-4
792 Mardia and Jupp (2000). Correlation and Regression. Directional Statistics. *West Sussex,*
793 *England: John Wiley & Sons Ltd*
794 Martínez M.L., Silva R., López-Portillo J., Feagin R.A., Martínez E. (2020). Coastal Ecosystems
795 as an Ecological Membrane. *Journal of Coastal Research ; 95* (SI): 97–101.
796 doi: 10.2112/SI95-019.1

Masselink, G., B. Castelle, T. Scott,G. Dodet, S. Suanez, D. Jackson, Floc'h, F., (2016). Extreme wave activity during 2013/2014 winter and morphological impacts along the Atlantic coast of Europe,*Geophys. Res.Lett., 43*, 2135–2143, doi:10.1002/2015GL067492

Masselink, Gerd, Tuck, M., McCall, R., van Dongeren, A., Ford, M., and Kench, P. (2019). Physical and Numerical Modeling of Infragravity Wave Generation and Transformation on Coral Reef Platforms. *Journal of Geophysical Research: Oceans*, *124* (3), 1410–1433. doi: 10.1029/2018JC014411

Melito, L., Parlagreco, L., Devoti, S., Brocchini, M., (2022). Wave- and tide-induced infragravity dynamics at an intermediate-to-dissipative microtidal beach. *Journal of Geophysical Research: Oceans*, *127*, e2021JC017980. https://doi. org/10.1029/2021JC017980

Moisan M., Delahaye T., Laigre T., Valentini N., (2021). – Suivi des échouages de sargasse et de l'évolution du trait de côte par caméra autonome en Guadeloupe : analyse des résultats et bilan des observations. Rapport final. BRGM/RP-712-FR, 67 p., 63 ill.

NHC (National Hurricane Center). (2021). HURRICANE TEDDY (AL202020). https://www.nhc.noaa.gov/data/tcr/AL202020_Teddy.pdf

Ning, Y., Liu, W., Sun, Z., Zhang, Y., (2019). Parametric study of solitary wave propagation and runup over fringing reefs based on a Boussinesq wave model. *J Mar Sci Technol 24*, 512–525. https://doi.org/10.1007/s00773-018-0571-1

Orejarena-Rondón, A F., Sayol, J. M., Marcos, M., Otero, L.,, Restrepo, J. C., Hernández-Carrasco, I., Orfila, A., (2019). *Front. Mar. Sci. 6* .2296-7745. 10.3389/fmars.2019.00614

Paquier, A.E., Laigre, T., Belon, R. Balouin, Y., Valentini, N, (2020). Video monitoring of Posidonia oceanica banquettes on pocket beaches, Northern Corsica. *XVIèmes journées nationales Génie Côtier - Génier Civil, Le Havre, France*. ⟨hal-02931679⟩

Pearson, S.G., Storlazzi, C.D., van Dongeren, A.R., Tissier, M.F.S., Reniers, A.J.H.M. (2017). A Bayesian-based system to assess wave-driven flooding hazards on coral reef- lined coasts. *Journal of Geophysical Research: Oceans*, *122* (12), 10099–10117. doi: 10.1002/2017JC013204

Péquignet, A., Becker, J., Merrifield, M., Aucan, J., (2009). Forcing of resonant modes on a fringing reef during tropical storm Man-yi. *Geophys. Res. Lett. 36*. doi: 10.1029/2008GL036259

Péquignet, A., M. Becker, N., J., and Merrifield, M. A., (2014). Energy transfer between wind waves and low- frequency oscillations on a fringing reef, Ipan, Guam, *Journal of Geophysical Research: Oceans*, *119*, 6709–6724, doi:10.1002/ 2014JC010179

Perry, C.T., Alvarez-Filip, L., Graham, N.A.J., Mumby, P.J., Wilson, S.K., Kench, P.S., et al. (2018). Loss of coral reef growth capacity to track future increases in sea level. *Nature, 558*(7710), 396-400. doi: 10.1038/s41586-018-0194-z

Plant, N.G., Aarninkhof, S.G.I, Turner, I.L., and Kingston, K.S, (2007). The performance of shoreline detection models applied to video imagery. *Journal of Coastal Research, 23*(3), 658–670. West Palm Beach (Florida), ISSN 0749-0208

Pomeroy, A., Lowe, R. J., Symonds, G., van Dongeren, A. R., and Moore, C. (2012). The dynamics of infragravity wave transformation over a fringing reef. *Journal of Geophysical Research, 117*, C11022. doi: 10.1029/2012JC008310

Quataert, E., Storlazzi, C., van Rooijen, A., Cheriton, O., van Dongeren, A. (2015). The influence of coral reefs and climate change on wave-driven flooding of tropical coastlines. *Geophys. Res. Lett. 42* (15), 6407–6415. doi: 10.1002/2015GL064861

Quataert, E., Storlazzi, C., van Dongeren, A., and McCall, R. (2020). The importance of explicitly modelling sea-swell waves for runup on reef-lined coasts. *Coastal Eng. 160*:103704. doi: 10.1016/j.coastaleng.2020. 103704

Reguero, B.G., Méndez, F.J., Losada, I.J., (2013). Variability of multivariate wave climate in Latin America and the Caribbean. *Global Planet Change, 100*, pp. 70-84

Rodríguez-Padilla, I., Castelle, B., Marieu, V., Bonneton, P., Mouragues, A., Martins, K., & Morichon, D. (2021). Wave-Filtered Surf Zone Circulation under High-Energy Waves Derived from Video-Based Optical Systems. *Remote Sensing, 13*(10), 1874

Roeber, V., and Bricker, J.D. (2015). Destructive tsunami-like wave generated by surf beat over a coral reef during Typhoon Haiyan. *Nature Communications 6*, 7854. doi: 530 10.1038/ncomms8854

Roelvink F.E., Storlazzi C.D., van Dongeren A.R. and Pearson S.G., (2021). Coral Reef Restorations Can Be Optimized to Reduce Coastal Flooding Hazards. *Front. Mar. Sci. 8*:653945. doi: 10.3389/fmars.2021.653945

Rueda, A., Vitousek, S., Camus, P., Tomás, A., Losada, I.J., Barnard, P.L., Erikson, L.H., Ruggiero, P., Reguero, P., Mendez, F.J., (2017). A global classification of coastal flood hazard climates associated with large-scale oceanographic forcing. *Sci Rep 7*, 5038 https://doi.org/10.1038/s41598-017-05090-w

Rueda, A., Cagigala, L., Pearson, S., Antolínez, J.A.A., Storlazzi, C., van Dongeren, A., Camuse, P., Mendez, F.J., (2019). HyCReWW: a hybrid coral reef wave and water level metamodel. *Comput. Geosci. 127*, 85–90. https://doi.org/10.1016/j. cageo.2019.03.004

Salmon, S.A., Bryan, K.R., Coco, G. (2007). The use of video systems to measure run-up on beaches. *J. Coast. Res. 50*, 211–215

SHOM (Service Hydrographique et Océanographique de la Marine), (2016). LITTO3D® Guadeloupe. https://services.data.shom.fr:/geonetwork/srv/api/records/BATHYMETRIE_LITTO3D_GUAD_2016.xml

SHOM (Service Hydrographique et Océanographique de la Marine), (2020). Références Altimétriques Maritimes - édition 2020. 126p

Slangen, A. B. A. , Carson, M, Katsman, C. A. , van de Wal, R. S. W. , Köhl, A,. Vermeersen, L. L. A, Stammer, D. , (2014). Projecting twenty-first century regional sea-level changes. *Clim. Change 124*, 317–332

Sous, D., Tissier, M., Rey, V., Touboul, J., Bouchette, F., Devenon, J.-L., Chevalier, C., and Aucan, J., (2019). Wave transformation over a barrier reef. *Continental Shelf Research, 184*:66–80

Spalding MD, Ruffo S, Lacambra C, Meliane I, Hale LZ, Shepard C., Beck M. (2014). The role of ecosystems in coastal protection: Adapting to climate change and coastal hazards. *Ocean & Coastal Management 90*: 50–57. doi: 10.1016%2Fj.ocecoaman.2013.09.007

Stammer, D.; Cazenave, A.; Ponte, R.M.; Tamisiea, M.E. (2013). Causes for Contemporary Regional Sea Level Changes. *Annu. Rev. Mar. Sci., 5*, 21–46

Storlazzi, C. D., Gingerich, S. B., van Dongeren, A. R., Cheriton, O. M., Swarzenski, P. W., Quataert, E., et al. (2018). Most atolls will be uninhabitable by the mid- 21st century because of sea-level rise exacerbating wave-driven fooding. *Sci. Adv. 4*, 1–10. doi: 10.1126/sciadv.aap9741

Symonds, G., Huntley, D. A., & Bowen, A. J. (1982). Two-dimensional surf beat: Long wave generation by a time-varying breakpoint. *Journal of Geophysical Research: Oceans, 87*(C1), 492–498. doi: 10.1029/JC087iC01p00492

Valentini, V., Saponieri, A., Danisi, A., Pratola, L., Damiani, L. (2019). Exploiting remote imagery in an embayed sandy beach for the validation of a runup model framework, *Estuarine, Coastal and Shelf Science, Volume 225*,106244, ISSN 0272-7714, doi: 10.1016/j.ecss.2019.106244

Valentini, N., Balouin, Y. (2020). Assessment of a Smartphone-Based Camera System for Coastal Image Segmentation and Sargassum monitoring *Journal of Marine Science and Engineering 8*, no. 1: 23. doi:10.3390/jmse8010023

Valentini, N., Balouin, Y. and Bouvier, C. (2020). Exploiting the capabilities of surfcam for coastal morphodynamics analysis. *Journal of Coastal Research SI95*: 1333-1338.

Valle-Levinson, A, Martin, J.B., (2020).Solar activity and lunar precessions influence extreme sea-level variability in the U.S. Atlantic and Gulf of Mexico coasts. *Geophys. Res. Lett., 47*, Article e2020GL090024

Vitousek, S.K., Barnard, P.L., Fletcher, C.H., Frazer, N., Erikson, L.H., Storlazzi, C.D. (2017). Exponential increase in coastal flooding frequency due to sea-level rise. *Nat. Sci. Rep. 7*, 1399. https://doi.org/10.1038/s41598-017-01362-7

Vetter, O., J. M. Becker, M. A. Merrifield, A.-C. Péquignet, J. Aucan, S. J. Boc, and C. E. Pollock (2010). Wave setup over a Pacific Island fringing reef, *Journal of Geophysical Research*, *115*, C12066, doi:10.1029/2010JC006455

Torres, R. R., and Tsimplis, M.N., (2012). Seasonal sea level cycle in the Caribbean Sea, *Journal of Geophysical Research: Oceans, 117*, C07011, doi:10.1029/2012JC008159.

Torres, R.R., & Tsimplis, M.N., (2013). Sea-level trends and interannual variability in the Caribbean Sea. *Journal of Geophysical Research: Oceans 118*(6), 2934-2947. doi: 10.1002/jgrc.20229

Wang, J., Church, J.A., Zhang, X., Chen, X., (2021). Reconciling global mean and regional sea level change in projections and observations. *Nat Commun 12*, 990 https://doi.org/10.1038/s41467-021-21265-6